DEVELOPMENT OF N-DOPED CARBON NANOMATERIALS WITH CONTROLLED SHAPE AND COMPOSITION FOR FUNDAMENTAL STUDIES OF ELECTROCATALYTIC SYSTEMS BASED ON PGM AND PGM-FREE CATALYSTS

by

Matthew B Strand

A thesis submitted to the Faculty and the Board of Trustees of the Colorado School of Mines in partial fulfillment of the requirements for the degree of Master of Science (Materials Science).

Golden, Colorado

Date: _____

Signed: _____

Matthew B Strand

Signed: _____

Dr. Svitlana Pylypenko
Thesis Advisor

Golden, Colorado

Date: _____

Signed: _____

Dr. Ryan O'Hayre
Professor and Head
Materials Science Program

ABSTRACT

Renewable energy technologies such as polymer electrolyte membrane fuel cells (PEMFCs) can potentially offset growing energy demands, however challenges such as cost and stability of oxygen reduction catalysts (ORR) remain to be addressed. Some of these challenges can be addressed by development of efficient catalysts and supports. Research has shown that stability of the platinum group metal (PGM) and PGM-free nanoparticle catalysts can be improved by modifying properties of the carbon support with nitrogen dopants. Development of more active and stable PGM-free catalysts such as those based on N-doped carbon and atomically dispersed iron species (Fe-N-Cs) would have drastic effect on the cost of the catalysts. Fundamental understanding of N-doped systems and their impact on performance of PGM and PGM-free catalysts can be advanced by utilizing novel characterization approaches and employing model high-surface area materials.

This work focuses on development of N-doped carbon nanospheres (N-CS) with controlled composition and shape to serve as model high-surface area substrates. In fabricated N-CS, it was found that both N at% and at% of pyridinic N species decrease as pyrolization temperature increases. N-CS in the range of 50-100 and 100-200 nm were selected as best candidates for use in further catalyst studies and were used to develop a series of model Fe-N-C nanospheres. Among Fe precursors used, $FeCl_3 \cdot 6\ H_2O$ resulted in the best dispersion of Fe, presumably as atomically dispersed species. Further, N-CS were used as substrates for Pt nanoparticle catalysts which were shown to contain 2-4 nm Pt nanoparticles dispersed over the surface of the N-CS substrate. The range of compositions of the series of developed materials demonstrates their applicability for future studies using novel *ex-situ* and *in-situ* methods.

TABLE OF CONTENTS

LIST OF FIGURES

LIST OF TABLES

ACKNOWLEDGEMENT

The research presented in this thesis was made possible thanks to the support and guidance I received over the years from many individuals. First and foremost, I acknowledge my advisor Dr. Svitlana Pylypenko for accepting me as her first graduate student. I am thankful for the guidance she provided in directing my research, as well as her excellent tutelage in developing many of my technical skills. To my thesis committee members, Drs. Ryan O'Hayre and Ryan Richards, I appreciate the feedback and comments provided for refining this thesis.

This work was also enhanced by contributions from members of the Pylypenko group: Dr. Chilan Ngo, Michael J. Dzara, Samuel Gage, Sarah Shulda, Caleb Stetson, and Natalie Seitzman. In particular, Michael Dzara acquired all XPS data on samples. Dr. Chilan Ngo acquired all EDS data and prepared all APT posts in addition to providing feedback for improvement of APT sample preparation. I am also indebted to the undergraduate research fellows who contributed their time and support in the lab and were instrumental in advancing my studies: Austin K. White and Jaime C. Hagen.

This work would not have been possible without the funding provided by the teaching assistanceship with the Colorado School of Mines Department of Chemistry. The assistanceship presented me with the opportunity to work with undergraduate students and further expand my teaching capabilities, in turn providing guidance on where and where not to direct my career in the future. Funding was also provided by the Trefny Institute through the Bechtel K-5 Educational Excellence Initiative grant. I thank Dr. Barbara Moskal for selecting me to become a fellow in this program, allowing me to practice STEM outreach for K-12 students.

I would also like to thank my family for their continued support during my graduate studies. I am grateful to my parents, Alan and Jane Strand, for raising me with the encouragement and morale fiber which motivated me to pursue higher education. The humor and energy of my sisters

Rebekah, Abigail, and Emily were also greatly appreciated. Finally, I would like to thank my friend and mentor G. Jeremy Leong for encouraging me to further my education and pursue graduate studies. I will be forever grateful for the opportunities for research and publication that were made possible through our interactions over the years.

CHAPTER 1

INTRODUCTION

1.1 Background and Motivation

Research into the development and improvement of alternative, renewable energy resources is of significant importance to the worldwide community as energy demands continue to grow. Polymer electrolyte membrane fuel cells (PEMFCs) are a promising technology for commercialization, though technical challenges must still be addressed to improve their economic viability. PEMFCs consist of a cathode and anode separated by an electrolytic membrane. Hydrogen oxidation reaction described by the half reaction $H_2 \rightarrow 2\ H^+ + 2\ e^-$ occurs at the anode: protons then migrate across the electrolyte membrane to reach the cathode. Here, the oxygen reduction reaction (ORR) described by the half reaction $O_2 + 2\ H^+ + 2\ e^- \rightarrow 2\ H_2O$ occurs. Both HOR and ORR utilize platinum group-based (PGM) catalysts, and one of the major challenges in improving economic viability of fuel cells results from the poor long-term stability of the catalyst and its reliance on scarce and expensive transition metals.

1.1.1 ORR Catalysts

ORR occurs very slowly in the absence of a catalyst, limiting total power density.[1] ORR is readily catalyzed by a variety of Pt and Pt alloy materials.[1–5] State of the art catalysts are based on carbon-supported Pt and PtCo nanoparticles.[3,5] Degradation of the catalysts occurs via dissolution/reprecipitation, migration/coalescence, and detachment during fuel cell operation due to corrosion.[6,7] During potential cycling, dissolution of Pt nanoparticles or of Pt oxides into the electrolyte causes a loss in electrochemical surface area (ECSA), resulting in loss of performance over the lifetime of the catalyst.[8,9] Dissolved Pt is deposited inside the fuel cell via two primary mechanisms: Ostwald ripening onto undissolved Pt nanoparticles, which results in increased

particle size, lower specific surface area, and thus lower ESCA; and reprecipitation onto the electrode, which may result in newly formed Pt nanoparticles being inaccessible to electrons, protons, or reactant gases. Migration is the process of catalyst nanoparticles moving across the surface of the support, and coalescence occurs when two or more nanoparticles meet, resulting in the formation of larger nanoparticles.[6,10,11] Finally, detachment occurs when the carbon support on which catalyst nanoparticles are mounted corrodes due to operating conditions of the fuel cell, causing nanoparticles to detach from the electrode.[12,13] The mechanism is generalized by the reaction: $C + 2H_2O \rightarrow CO_2 + 4H^+ + 4e^-$.[13]

Alloying Pt with other metals (mainly Co or Ni) has the potential to improve its activity as well as stability in the acidic environment of the PEMFC.[3-5,14–18] Improvements to activity for ORR can be explained in part by the change in Pt-Pt interatomic distance caused by alloying with other metals.[14] Schenk and coworkers describe an economic and flexible manufacturing process investigating PtCo electrode assemblies for ORR characterized by both *in situ* and *ex situ* electrochemical measurements. Under a variety of tested conditions, the synthesized catalyst showed equal specific performance to a commercially available Pt catalyst; however, it utilized a lower weight% of Pt.[3] Jorné and coworkers investigated the electrochemical activity of Pt supported on Vulcan carbon (Pt/V) and PtCo supported on high surface area carbon (PtCo/HSC) using rotating disk electrode (RDE) and membrane electrode assembly (MEA) methods. The specific activity of both catalysts decayed over time and was primarily attributed to catalyst degradation, which occurred more rapidly on the PtCo/HSC.[1] While formation of an oxide layer on the surface of the catalyst also contributed to the decay, the initial activity of PtCo/HSC was higher than that of Pt/V and remained higher over the duration of testing, indicating that catalytic activity depends on a variety of factors and cannot only be attributed to presence of an oxide layer.

Core-shell materials have also been utilized to improve stability for Pt-based catalysts while maintaining high activity.[2,19] Adzic and coworkers describe a synthesis of Pd core/Pt monolayer shell catalysts mounted on carbon support (PtML/Pd/C) and performed electrochemical measurements of their activity for ORR. Accelerated fuel cell stability testing was performed for 100,000 cycles: loss of Pt from PtML/PdAu/C catalyst was negligible, and the mass activity decreased by 37% compared to the 68% observed for commercially available Pt/C. Pt dissolution was mitigated due to the Pd core, which dissolved and diffused away from the cathode toward the anode. Stability of the Pd core was further improved by addition of Au to yield a Pd_9Au_1 core, which slowed Pd oxide formation and dissolution.

While PGM catalysts have the best performance for ORR, high cost and limited availability of the catalyst hinders the economic viability of their widespread use.[20] Utilization of PGM-free catalysts which exhibit activity towards ORR would significantly reduce costs associated with PEMFCs.[21,22] Some of the most commonly researched PGM-free catalysts are based on Fe[23–30] or Co.[29–32] Some of the PGM-free catalysts are based on carbon supported PGM-free nanoparticles and they are typically design for use in alkaline environment due to very limited activity and stability in acid media. The most promising class of PGM-free catalysts in acidic environment is based on N-doped carbon network functionalized with atomically dispersed iron.[21,23]

1.1.2 Catalyst Supports

High surface area carbon is utilized as a state-of-the-art support for both PGM and PGM-free catalysts. One of the main advantages of employing a high surface area support is opportunity to disperse metal phase and therefore increase active surface area of the catalyst. Carbon-supported Pt and Pt alloy catalysts have excellent active surface area and mass activity for ORR, but degradation of the catalyst limits their effective life cycle. Typical carbon supports used in state-of-the art catalysts are Vulcan black, Ketjen black and their graphitized versions.

Researchers have been actively pursuing development of novel carbon supports with improved corrosion stability and enhanced catalyst-support interactions.[33–36] Peng and coworkers reduced Pt onto carbon nanotubes (CNTs) to synthesize a Pt/CNT catalyst and tested its activity for both ORR and methanol oxidation reaction (MOR).[33] Cyclic voltammetry revealed that specific activity for ORR decreases as the weight% of Pt increases, while the specific activity for MOR increases slightly, suggesting that ORR is limited by mass transfer at high Pt loadings while MOR is limited by proton conduction. Durability testing of Pt nanoparticles mounted on multi-wall CNTs (MWCNTs) in comparison to a commercially available Pt on Vulcan carbon (Pt/XC72) catalyst was conducted by Shiroishi and coworkers.[35] Though the synthesized Pt/MWCNT catalysts had lower electrochemical surface area and initial current flow for ORR, they retained their activity for a greater period of time than the commercially available catalyst, suggesting that an interaction between the graphitic support and Pt nanoparticles is responsible for increased stability. Stability of Pt on graphitic catalysts was elucidated by Lu and coworkers by depositing Pt on graphene, followed by addition of glucose and carbonization.[36] Cyclic voltammetry and RDE measurements of the synthesized catalyst indicated it had similar activity for ORR as a commercially available Pt/C catalyst, but retained more of its activity after 10,000 cycles due to the graphitic support and coating. When graphitization was not performed, no significant activity was observed as the non-graphitic carbon coated the active site on the Pt nanoparticles.

1.2 Electrocatalysts based on Nanoparticles Supported on N-doped Carbons

Research has shown that the presence of dopants such as nitrogen can modify properties of carbon supports with benefits related to catalyst dispersion, activity and stability.[29,37,38] The interplay between nitrogen concentration and specific nitrogen functionalities and their effect on catalyst-support interactions is still not completely understood due to heterogeneous nature of N-doped carbons. Since catalysis of ORR cannot occur if the active site is covered, both stability

from interactions between Pt and the support and activity from exposed surface area of the nanoparticles must be optimized. Carbon supports treated with a variety of other dopants such as F, P, or S have demonstrated improved stability over pure graphitic supports.[39–45]

1.2.1 PGM Nanoparticle Catalysts Supported on N-doped Carbon

Sun and coworkers reported on the impact of N-dopants on Pt deposited on N-doped CNTs (Pt/CN_x), analyzing materials prepared with different N at% to evaluate Pt nanoparticle dispersion and catalyst durability.[39] TEM of Pt/CN_x shown in Figure 1.2 demonstrate improved dispersion of Pt nanoparticles as N at% increases, and was attributed to increased number of surface defects. Accelerated durability testing was also performed, with Pt/N-CNTs doped with 8.4 at% N retaining 42.5% of their ECSA after 4000 cycles while commercially available Pt/C only retained 4.6%.

Shanmugam and coworkers investigated the effect of N doping of Pt/graphene on ORR activity, using $Gd_2O_2CO_3$ and Gd_2O_3 as sacrificial templates to prepare carbon supports.[42] X-ray photoelectron spectroscopy (XPS) characterization indicated the presence of pyridinic, pyrrolic, and graphitic N in the carbon material, with a higher frequency of pyridinic N in the $Gd_2O_2CO_3$ material. This corresponded to a 30 mV increase in half-wave potential for ORR, as well as specific activity of 157 mA mg_{Pt}^{-1} compared to 84.1, suggesting the interaction between pyridinic N and Pt has a favorable contribution to ORR activity.

Chen and coworkers mounted Pt nanoparticles on S-doped graphene sheets (Pt/SG) and subjected it and commercially available Pt/C and Pt on graphene (Pt/G) to electrochemical cycling on a RDE.[41] Both Pt/SG and Pt/G demonstrated higher stability than Pt/C after 1500 cycles, and Pt/SG had the highest initial specific activity for ORR at 139 mA mg_{Pt}^{-1} compared to 101 and 121 mA mg_{Pt}^{-1} for Pt/G and Pt/C, respectively. In addition, it had the highest sustained activity after 1500 cycles with a half-wave potential loss of only 11 mV, compared to 23 and 43 mV for Pt/G and Pt/C, respectively. Computational modeling of S dopants on the graphene indicate the

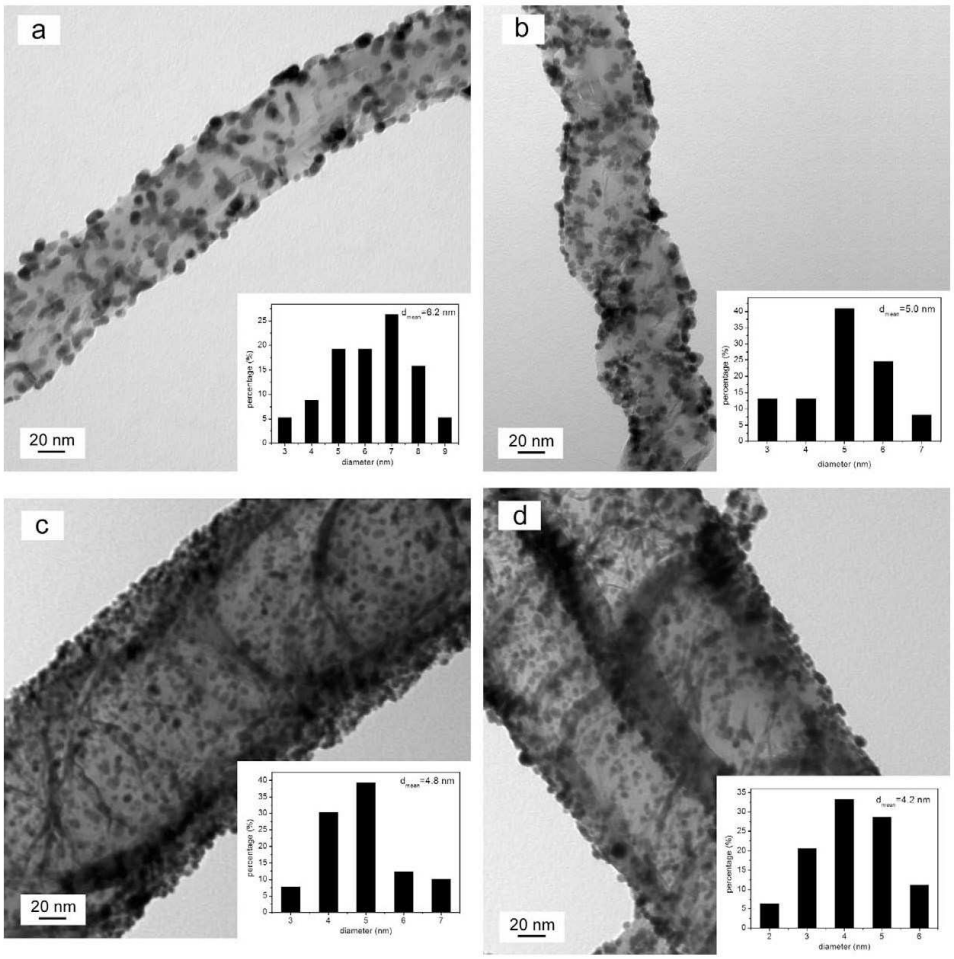

Figure 1.1 TEM images and size distribution histograms (insets) of original Pt nanoparticles deposited on: (a) CNTs, (b) CN_x (1.5 at% N), (c) CN_x (5.4 at% N) and (d) CN_x (8.4 at% N) (ref 39).

improved stability and activity can be attributed to interactions between S and the Pt nanoparticles. CNTs co-doped with N and P also show promise as a support for Pt for ORR.[44] Peng and coworkers synthesized graphene doped with N, P, and both N and P, then performed cyclic voltammetry and linear sweep voltammetry on each. While specific current densities of all three materials were very similar, the half-wave potential of the NP-doped catalyst was greater than that of the N- or P-doped catalysts. Additionally, the NP-doped catalyst lost only 0.06 V of half-wave potential and 42% of its peak current after 6000 cycles, compared to the 0.27 V and 63.5% loss of the P-doped

catalyst after only 3000 cycles. DFT calculations were performed to investigate the interactions between P, N, and Pt atoms to identify possible binding sites and energies.

1.2.2 PGM-free Catalysts Based on Carbon, Nitrogen, and Atomically Dispersed Iron

Lefèvre and coworkers prepared an Fe-based catalyst on microporous carbon doped with N (Fe-based NPMC).[23] The best-performing catalyst exhibited a volumetric activity for ORR of 99 A cm^{-3}, nearly 35 times more catalytically active than previously reported Fe-based catalysts and within 10% of the activity of Pt-based catalysts. The high activity was attributed to a high number of active sites: at each site, four pyridinic N functionalities located at edges of the carbon network coordinate an Fe^{2+} cation. Durability tests were conducted over 100 hours and demonstrated the material had higher overall current densities than previous PGM-free catalysts, although a greater relative loss of activity was observed which indicated a lack of stability.

Zelenay and coworkers synthesized an Fe-based PGM-free catalyst via incorporation of $FeCl_3$ and aniline into commercially available Ketjen black and evaluated their performance for ORR with a rotating disk electrode (RDE).[26] The best performing catalyst was obtained by heat-treating at high temperatures (900 °C) to incorporate more Fe, resulting in the largest number of Fe-N_xC_y centers as determined by X-ray absorption near-edge structure spectroscopy (XANES). Principle component analysis was utilized to correlate ORR activity with total amount of Fe-N, quaternary and graphitic N, ratio of pyrrolic N to N-Fe, and to surface area found from BET.

Mukerjee and coworkers reported preparation of Fe-N-C materials for ORR from metal-organic frameworks (MOFs), specifically by ball-milling ZIF-8 MOF with $Fe(acetate)_2$ and 1,10-phenthroline monohydrate then heat-treating under Ar and then NH_3.[28] The material demonstrated high current density of 50 mA cm^{-2} due to a high number of Fe-N_4 active sites, and the role of Fe oxidation state in Fe-catalyzed ORR was elucidated by XANES and *ex-situ* Mössbauer

spectroscopy. Their results suggest that the high activity of MOF-based Fe-N-C catalysts primarily results from the disordered carbon matrix in which Fe moieties are embedded.

Atanassov and coworkers utilized sacrificial silica templates to produce Fe-based catalysts for ORR using nicarbazin, a charge transfer salt not previously used in such syntheses, as a nitrogen-carbon source (Fe-NCB).[37] Cab-O-Sil silica was selected as template to maximize the number of defects in the carbon matrix, previously shown to facilitate formation of Fe-N_xC_y active sites. When subjected to several durability testing procedures on RDE, the Fe-NCB was found to lose only 3-4% of its initial current density. MEAs were prepared, and best performance of 100 mA cm^{-2} was achieved when 55 wt% Nafion was used with the Fe-NCB.1.3 Motivation for Study

While PGM-free catalysts are a promising technology that avoids the high cost and limited availability of PGM catalysts, their active site is difficult to characterize due to high heterogeneity of materials. Well-studied model substrates such as highly oriented pyrolytic graphite (HOPG) cannot be directly used as a support in fuel cells. As such, the role of N in activity and stability of N-doped supports for both PGM and PGM-free catalysts requires further study. Understanding of the role of N can be achieved by examining atomic and 3D composition and structure of model materials, and the interactions of those materials with PGM-free catalysts in which the catalyst is atomically dispersed. In-situ TEM can grant insight into dispersion across the N-doped substrate, and electrochemistry can correlate changes in composition and morphology with performance.

1.3 Goals and Structure of Thesis

The work described in this thesis focuses on development of nitrogen-doped carbon nanospheres (N-CS) to serve as model high-surface area substrates. N-CS are an ideal model substrate for several reasons: first, the composition of the N-CS can be readily controlled through alterations to the synthesis procedure, facilitating investigation of the role of different N functionalities. Second, size of the discrete nanospheres can be altered to allow for analysis by

novel methods such as atom probe tomography (APT) and in-situ TEM. Third, the synthesis method can be scaled up in order to produce sufficient material for all characterization techniques to be performed on a single, homogeneous batch of N-CS. There were four sets of objectives for the work described in this thesis:

1. Development of model high-surface area N-doped carbons with controlled shape and composition;
2. Development of model Fe-N-C catalysts with controlled shape and composition;
3. Development of model Pt/N-C materials with controlled shape and composition;
4. Investigation of control of catalyst composition when using SGD synthesis methods

1.4 Expected Impact

Development of model high-surface area N-doped carbon supports will allow fundamental studies of catalyst-support interactions in carbon supported nanoparticle catalysts for a wide range of metal catalyst nanoparticles, including Pt, PtCo alloy, and PtCo core-shell. In addition, interactions between N-doped support with nanoparticles derived by SGD synthesis methods could be investigated. Improved fundamental understanding of SGD mechanism will allow for better control of synthesis of new catalysts.

Additionally, N-doped carbon and N-doped carbons functionalized with Fe will be used as model substrates for elucidation of ORR on these materials. This specific system will allow for nanometer, atomic scale, and 3D characterization of this important class of materials.

CHAPTER 2

DEVELOPMENT OF MODEL HIGH SURFACE AREA N-DOPED CARBONS WITH CONTROLLED SHAPE AND COMPOSITION

2.1 Introduction

Fundamental understanding of N-doped systems and their impact on performance of platinum group metal (PGM) and PGM-free catalysts can be advanced by utilizing model high-surface area materials and multi-technique characterization approaches. In this chapter, a series of nitrogen-doped carbon nanospheres (N-CS) was developed to serve as model high-surface area substrates. The main objectives of this work are:

1. Synthesis of the N-CS material to create chemistries relevant to those observed in N-doped carbon supports and FeNC catalysts;

2. Synthesis of the N-CS maerial with controlled shape and size to enable novel characterization approaches, namely *in situ* transmission electron microscopy (TEM) and atom probe tomography (APT);

3. Preparation of both platinum-based and PGM-free catalysts to investigate the role of nitrogen in enhancing performance of catalysts for the oxygen reduction reaction (ORR), in particular their activity and stability.

A set of N-CS materials was prepared by modifying a previously published phenolic resin synthesis in which the amount of nitrogen was varied by tuning concentration of ethylenediamine (EDA), and distribution of nitrogen functionalities was varied by adjusting range of pyrolysis temperatures. Size control of N-CS was also accomplished by tuning concentration of ethylenediamine (EDA).

2.2 Solvothermal Synthesis of N-Doped Carbon Nanospheres and Scale-up

The preparation of N-CS was modified from a previously reported sol-gel synthesis.[46] Initial synthesis was performed via dissolution of reagents in an aqueous alcohol solution that was transferred into a 125 mL Teflon bomb and sealed inside a metal autoclave before subjecting to solvothermal conditions for 24 hours. To obtain sufficient quantities of each N-CS sample for all analytical techniques and for all further synthesis, multiple batches of the same samples needed to be prepared. To maintain consistency between samples and avoid deviations, the synthesis was scaled up by a factor of eight, utilizing a 1 L high-density polyethylene (HDPE) screwcap bottle instead of an autoclave.

For the synthesis of N-CS using 1 L bottles the following procedure was followed. Briefly, 3.200 g of resorcinol (Sigma Aldrich, >99%) was dissolved in an aqueous alcohol solution prepared from 320 mL of H_2O (18.2 MΩ) and 128 mL of ethanol (Pharmco-Aaper, 200 proof absolute anhydrous) in a 1 L HDPE screwcap bottle while stirring at 300 RPM. A variable volume of EDA (Sigma Aldrich, >99.5%) was added while stirring, followed by 4.800 mL of formaldehyde (Alfa Aesar, 37 wt%). Previous work has shown that controlling the concentration of base present in preparation of a resorcinol-formaldehyde resin inversely affects the size of the produced spheres.[46,47] EDA volumes of 1.600, 3.200, 4.800, and 6.000 mL correspond to 0.35, 0.70, 1.05, and 1.31 vol% of total solution volume, respectively. In this work, 5.400 mL EDA (1.18 vol%) samples were also prepared in order to obtain N-CS of a size intermediate to the 1.05 and 1.31 vol% samples.

Stirring continued for 24 hours after formaldehyde addition, then the stir bar was removed and bottle's lip wrapped with DuraFilm to ensure a gas-tight seal. Solvothermal conditions were achieved by placing the bottle in an oven at 100 °C for 24 hours, then removing and cooling the bottle under running tap water. Polymerized spheres (PS) were isolated by centrifugation of the

reaction mixture at 9000 RPM (9327 g) in a Marathon 22kbr centrifuge for 20 minutes, followed by aspiration of excess solution. The PS were then redispersed in ethanol, transferred into quartz boats, and air-dried at 70 °C for 12 hours to drive off ethanol. PS were then pulverized into a fine powder via a mortar and pestle to ensure uniform treatment during pyrolization.

Pyrolysis of PS was accomplished via thermal treatment at variable temperatures under N_2 (General Air, UHP) flowing at 100 sccm for the duration of the pyrolysis. A quartz boat containing PS was heated at 2 °C/min to 350 °C, dwelled for 4 hours, then heated at 5 °C/min to 600, 700, 800, or 900 °C. After dwelling for 2 hours, the oven was allowed to cool to 100 °C, then the N-CS were removed and transferred to a 20 mL scintillation vial for storage. Samples were prepared at different pyrolization temperatures in order to observe the effect of the heat treatment on both N at% and speciation of N present in the spheres.

Inital scale-up efforts used a 500 mL polypropylene (PP) bottle, while the second set of scale-ups used a 1 L HDPE bottle. All reactants were increased by the same factor to maintain concentrations: 3.200 g of resorcinol, 320 mL of H_2O, 128 mL of ethanol, 5.400 mL of EDA for 1.18 vol%, and 4.800 mL of formaldehyde were used. All other synthesis steps and parameters were identical to those described above.

Several factors were found to impact reproducibility and monodispersity of N-CS. It was observed that solvent would evaporate from the PP bottle during the solvothermal treatment, indicating that solvothermal conditions were not achieved for the full 24 hours which impacts the formation of polymerized spheres. Use of HDPE instead of PP mitigated effusion of solvent vapor during the solvothermal treatment, thereby maintaining solvothermal conditions. Average yield from 1 L syntheses was roughly equivalent to twice the average yield of 500 mL syntheses,

indicating that scale-up of the synthesis could be used to obtain sufficient quantities of each sample for all characterization and synthesis methods.

Further scale-up syntheses were performed using 2 L HDPE bottles, a 2x scale-up from the 1 L synthesis. For these, 6.400 g resorcinol, 640 mL H_2O, 256 mL ethanol, 10.800 mL EDA for 1.18 vol%, and 9.600 mL formaldehyde were used. Average yields for each scale-up again increased by the same factor.

2.3 Physiochemical Characterization

TEM images were obtained using a Philips CM200 instrument operated at 200 keV. Samples were prepared for imaging by dispersing 0.1 mg of N-CS in 1 mL of ethanol and sonicating for 10 minutes, then dropping 5 μL of solution onto a 300 mesh copper grid with lacey carbon backing (Ted Pella, 01895). The solution was aspirated after 15 seconds, and the grid was allowed to dry. Elemental mapping via energy dispersive X-ray spectroscopy (EDS) was conducted on a FEI Talos 200 FX scanning TEM operating at 200 keV with acquisition time of 10 minutes. XPS was performed on a Kratos AXIS Nova photoelectron spectrometer using a monochromatic Al Kα source operating at 300 W. The operating pressure was 2×10^{-9} Torr, and the photon energy 1486.6 eV. Survey and high-resolution spectra were acquired at pass energies of 160 eV and 20 eV, respectively. Samples were typically mounted on conductive carbon tape or a non-conducting tape in which case charge compensation with low energy electrons was applied when necessary. Typically, two spots on each sample were measured. High-resolution spectra were recorded for the C 1s, O 1s, and N 1s. XPS data was processed using CasaXPS software using a linear background subtraction for quantification of C 1s, O 1s, and N 1s. Peak fitting was performed using a series of components with a 70% Gaussian, 30% Lorentzian line shape.

2.3.1 TEM

TEM images of N-CS are shown in Figure 2.1 and possess comparable diameters (Table 2.1) to those produced via the original method with the same vol% EDA. By contrast, variation of upper pyrolization temperature from 600 to 900 °C did not cause significant variation in diameter. N-CS with 1.18 vol% EDA were prepared to obtain a series of samples with average sizes intermediate to those of 1.05 and 1.31 vol% EDA N-CS since characterization by *in situ* TEM utilizes a holder with narrow viewing window of <1 μm thickness. Particles of large diameter are thus at increased risk of agglomerating and damaging the window, while small particles lack sufficient contrast with the medium flowing in the holder. As 1.18 vol% EDA N-CS possess an average diameter of 200 nm as shown in Figure 2.2, they were selected for further scale-up and analysis. Several factors were found to impact reproducibility of N-CS: a delay between dispersion of PS in ethanol after cleaning, and drying ethanol away caused an increase in N-CS sizes and in sample polydispersity. Similar effects were seen when EDA used in the synthesis was repeatedly exposed to atmosphere, and was mitigated by utilizing reagent bottles fitted with a SureSeal.

Table 2.1 Particle size and standard deviation of pyrolized N-CS obtained from TEM images. All dimensions are in nanometers.

vol% EDA	**Upper Pyrolization Temperature (°C)**			
	600	**700**	**800**	**900**
0.35%	700-1500	700-1500	800-1500	800-1500
0.70%	500-600	500-600	500-600	500-600
1.05%	350-500	350-500	350-500	350-500
1.18%	150-250	150-250	150-250	150-250
1.31%	50-100	50-100	50-100	50-100

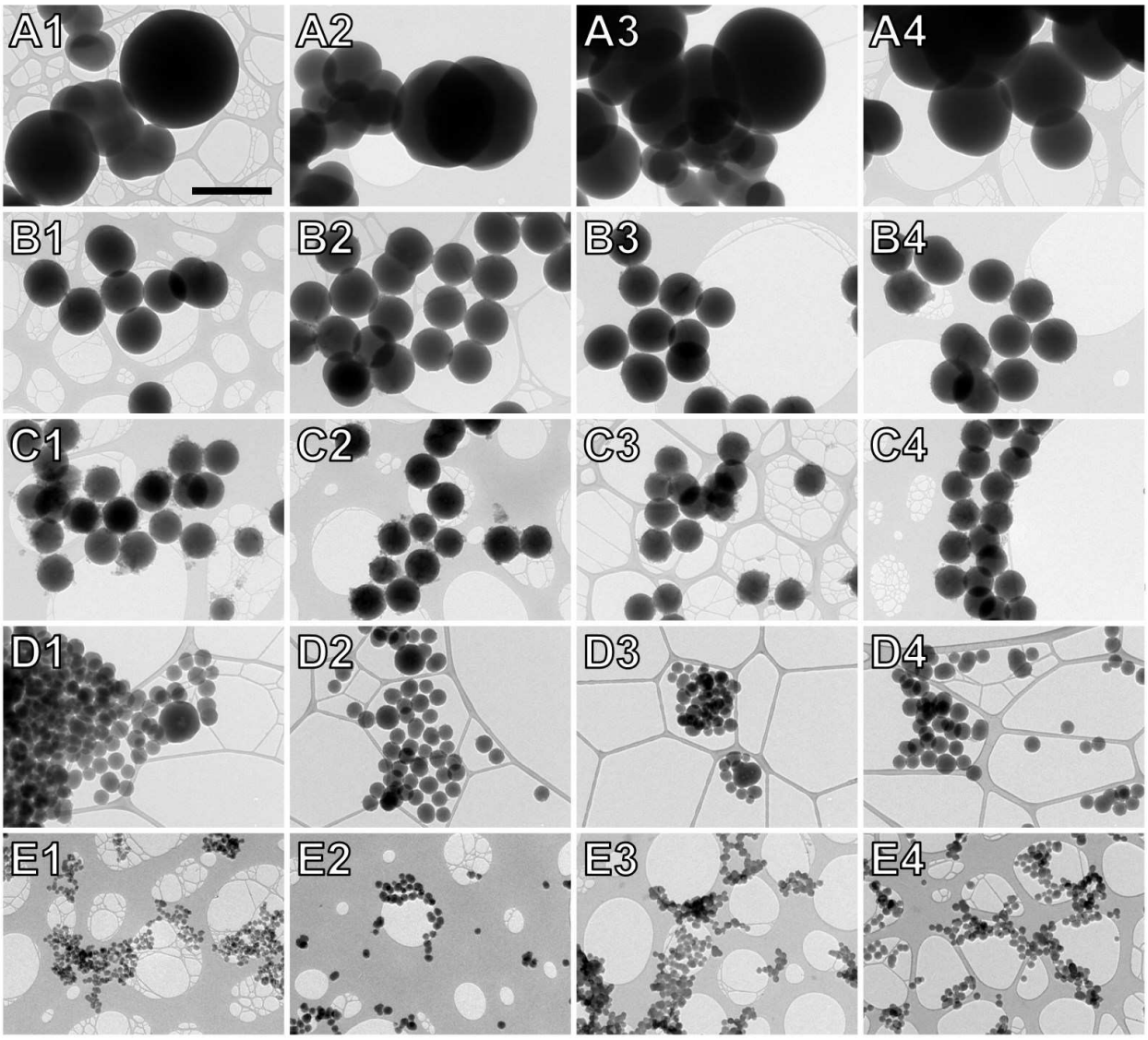

Figure 2.1 TEM of N-CS after pyrolization in flowing N_2. Increasing vol% EDA from 0.35 (A) to 0.70 (B), 1.05 (C), 1.18 (D), or 1.31 (E) yielded N-CS of decreasing diameter. Pyrolization temperatures of 600 (1), 700 (2), 800 (3), and 900 °C (4) did not significantly impact diameter. Scalebar is 1 μm, and all images were taken at the same magnification.

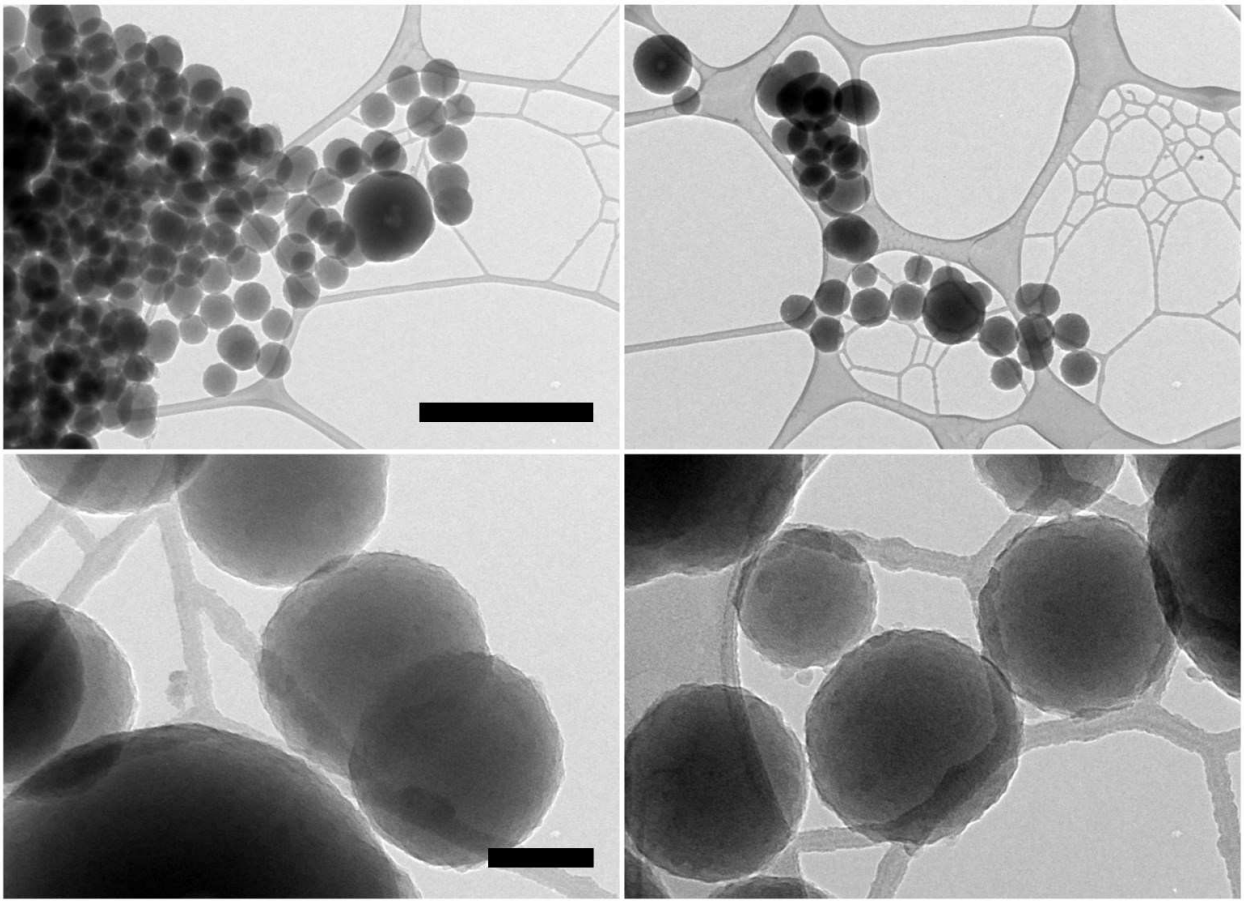

Figure 2.2 TEM of N-CS prepared with 1.18 vol% EDA and pyrolization temperature of 600 °C. Top scalebar is 1 μm, bottom scalebar is 100 nm.

2.3.2 Elemental mapping

The pyrolization of PS to yield N-CS has been previously shown to impact concentration of N,[3] suggesting that pyrolization influences the incorporation of N into the C framework. EDS was conducted on a series of 1.18 vol% EDA N-CS pyrolyzed at 600, 700, and 900 °C in order to correlate C, N, and O at% with changes in upper pyrolization temperature. Elemental maps of C and N are shown in Figure 2.3, demonstrating that N is well-dispersed throughout the N-CS. As seen in Table 2.2, increasing pyrolization T causes a decrease of N at%. Trace at% of Cu, Si, and Cl occur primarily from the Cu grid and backing on which the N-CS were mounted.

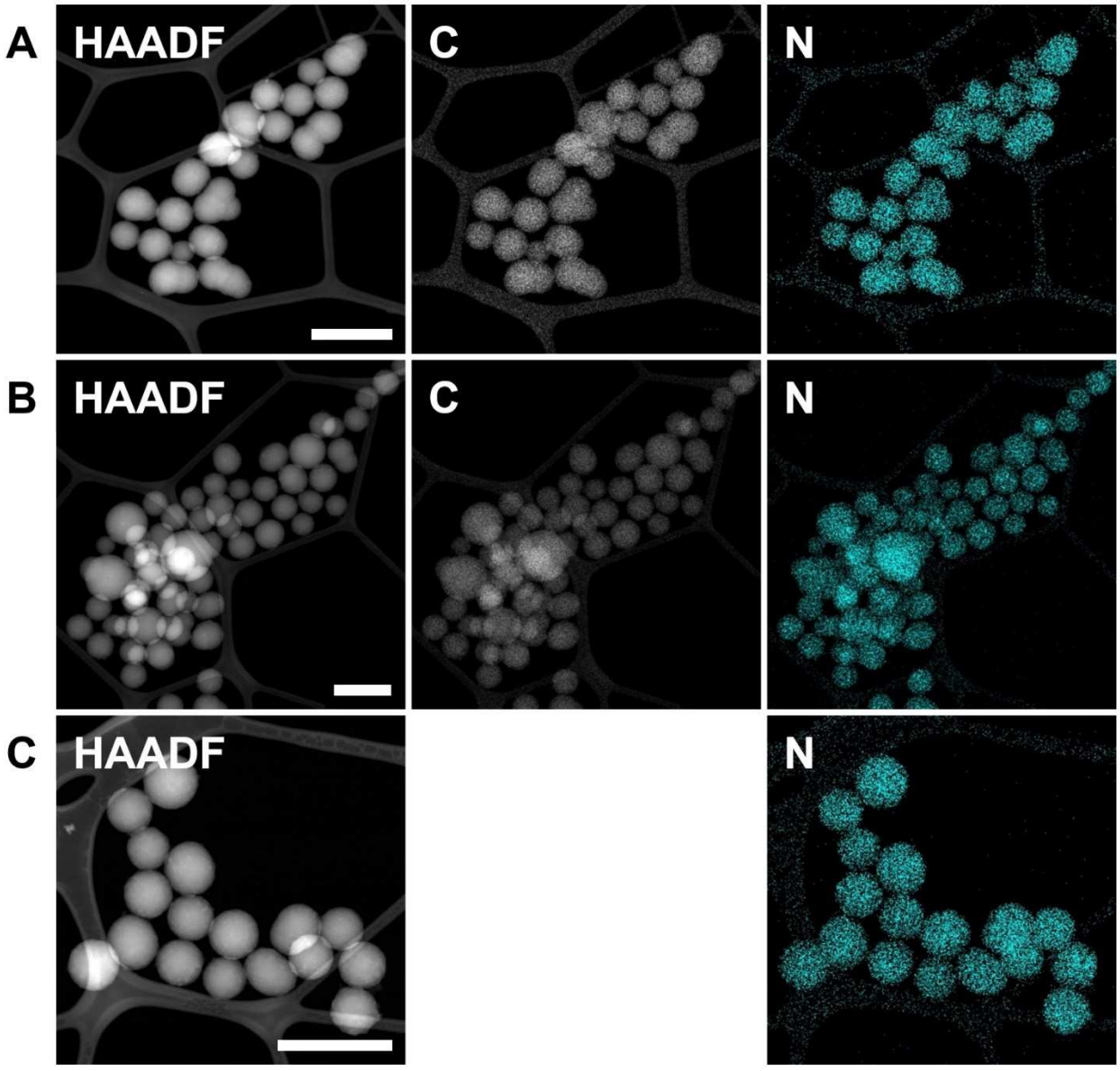

Figure 2.3 EDS elemental mapping of 1.18 vol% EDA N-CS. Samples were prepared at pyrolization temperatures of 600 (A), 700 (B), and 900 °C (C). HAADF images (left) as well as C (center) and N (right) maps are shown for each sample, although a C map was not collected for the 900 °C sample. Scalebars are 500 nm, and all images on the same row were taken at the same magnification.

Table 2.2 Elemental composition of 1.18 vol% EDA N-CS pyrolized at 600, 700, and 900 °C.

Element	Upper Pyrolization Temperature (°C)					
	600		700		900	
	at%	at% error	at%	at% error	at%	at% error
C	94.0	2.9	94.8	2.9	96.4	2.9
N	3.5	0.1	3.3	0.1	1.4	0.1
O	2.1	0.09	1.6	0.1	1.7	0.1
Cu	0.3	0.02	0.2	0.01	0.3	0.01
Cl	0.05	0.01	0.05	0.01	0.03	0.01
Si	0.01	0.02	0.01	0.02	0.1	0.01

2.3.3 X-ray Photoelectron Spectroscopy

High-resolution XPS spectra of 1.18 and 1.31 vol% EDA N-CS were analyzed via CasaXPS software: a linear background was fitted to high-resolution spectra of C 1s, O 1s, and N 1s measured from each sample. Spectra of 0.35, 0.70, 1.05, and 1.31 vol% EDA N-CS were acquired from samples mounted on non-conductive tape. In order to compare binding energies (BE) of components for the N 1s spectra, the samples were all charge referenced by calibrating the spectra so the C 1s peak occurred at 285.0 eV. However, several samples underwent charging during data collection, skewing collected spectra. Thus, all 1.18 vol% EDA N-CS were mounted on conductive tape and thus did not require calibration, resulting in a BE of 284.5 eV for the C 1s peak.

The relative at% of C, O, and N for each N-CS sample were obtained from the relative areas of regions fitted to each high-resolution spectra and are shown in Table 2.3. For both N-CS series, an increase in pyrolization temperature correlated to a decrease in both O at% and N at%: from 3.0 to 2.4 and 3.3 to 2.3 at%, respectively. The O at% from XPS was slightly higher than that

found from EDS, suggesting the surface of the N-CS was enriched with O relative to the entire particle. EDS and XPS also differed for N at%, but to a less significant degree.

Table 2.3 N at% determined from N 1s XPS spectra of N-CS. Components indicate presence of N species determined from their binding energy:

Element	Binding Energy (eV)	1.18 vol% EDA				1.31 vol% EDA			
		600	700	800	900	600	700	800	900
C	-	**93.74**	**93.46**	**94.33**	**95.38**	**92.61**	**93.69**	**94.31**	**95.34**
O	-	**2.95**	**3.58**	**2.90**	**2.36**	**4.16**	**3.32**	**3.35**	**2.74**
N	-	**3.32**	**2.99**	**2.78**	**2.27**	**3.23**	**2.99**	**2.34**	**1.91**
Nitridic	397.2	-	-	-	-	-	-	-	0.11
Pyridinic	397.8	0.35	0.61	0.46	0.32	0.48	0.48	0.49	0.24
	398.3	1.02	0.45	0.44	0.23	0.77	0.55	0.30	0.18
Pyrrolic	399.3	0.24	0.22	0.27	0.10	0.35	0.33	0.25	0.11
	400.1	0.61	0.51	0.37	0.21	0.54	0.44	0.30	0.18
Graphitic/	400.8	0.80	0.79	0.81	0.78	0.79	0.82	0.69	0.66
Quaternary	401.6	0.20	0.29	0.31	0.36	0.19	0.29	0.23	0.32
	402.5	0.10	0.13	0.12	0.25	0.10	0.10	0.08	0.10

Components were fit to all N 1s spectra using an fwhm of 1.0 eV and are shown in Figure 2.4. Each component fitted to the high-resolution N 1s spectra can be assigned to a specific N functional group. The relative area of each peak was used to determine relative concentrations of N species observed at various binding energies and are shown in Figure 2.5. Peaks at low binding energy (BE) typically occur due to pyridinic N (397.5-398.5 eV), while those at higher BE result from pyrrolic (399-401 eV) or graphitic/quaternary N (400.5-402.5 eV).[21, 48 – 51] The fitted components indicate that the loss of N at% with increasing pyrolization T is accompanied by a decrease in the pyridinic species at 398.3 eV and pyrrolic species at 399.3 and 400.1 eV. By contrast, a slight increase in N at% was observed for the graphitic/quaternary species at 401.6 eV. The 1.31 vol% EDA N-CS pyrolyzed at 900 °C was also observed to develop a new peak at 397.2 eV, not observed in all other samples, and its binding energy suggests the presence of nitridic species. Based on the fits of N 1s spectra, it can be concluded that the speciation of N in N-CS can be controlled by varying pyrolization temperature during synthesis. Prior studies indicate that

pyridinic N functionalities are most beneficial for improving stability of carbon supports used in fuel cells,[29,37,38,48] so the N-CS materials prepared here are ideal for use as supports for preparation of PGM and PGM-free catalyst materials to investigate the role of N functionalities.

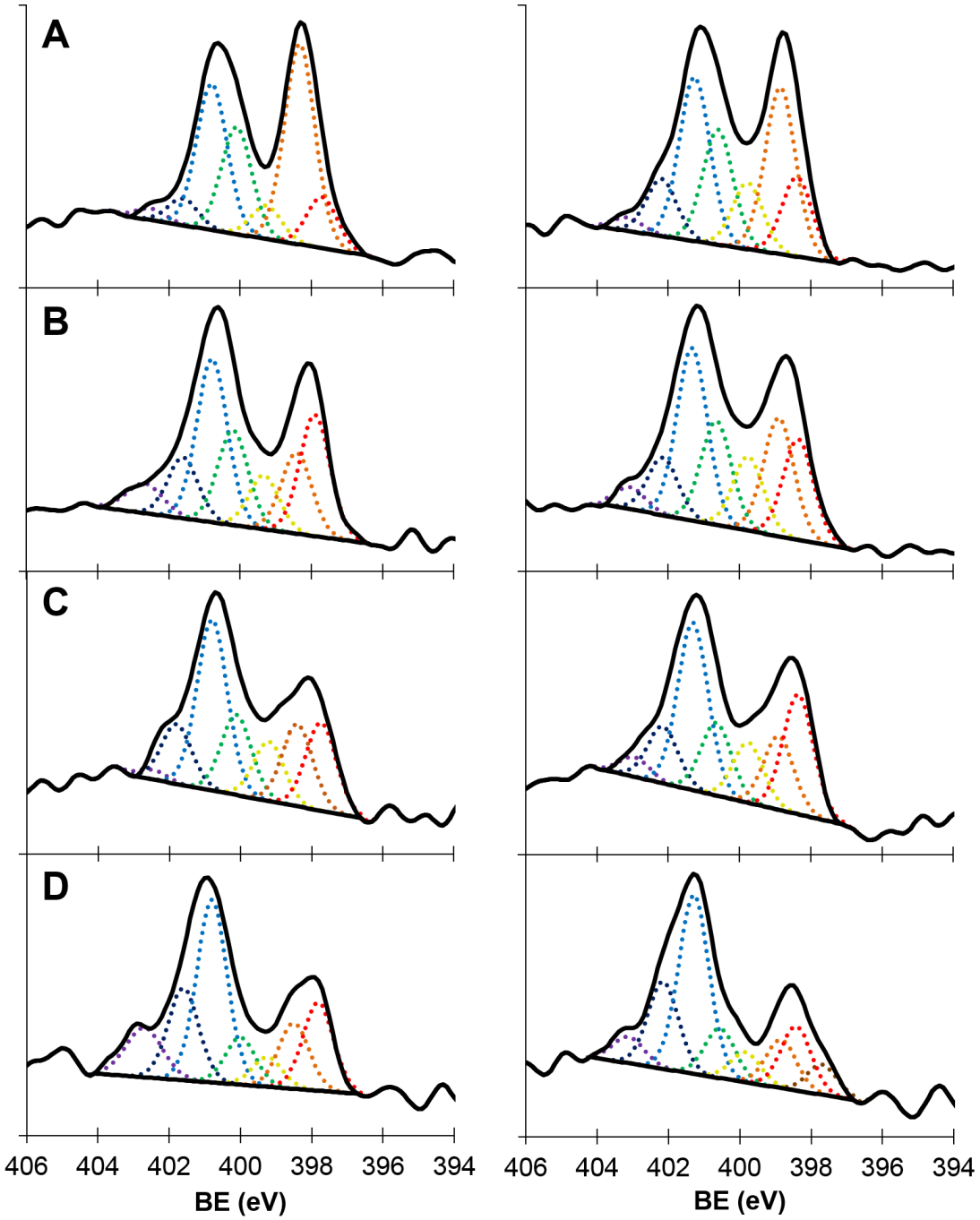

Figure 2.4 N 1s XPS spectra of N-CS made with 1.18 (left) and 1.31 vol% EDA (right). Spectra correspond to pyrolization temperatures of 600 (A), 700 (B), 800 (C), and 900 °C (D).

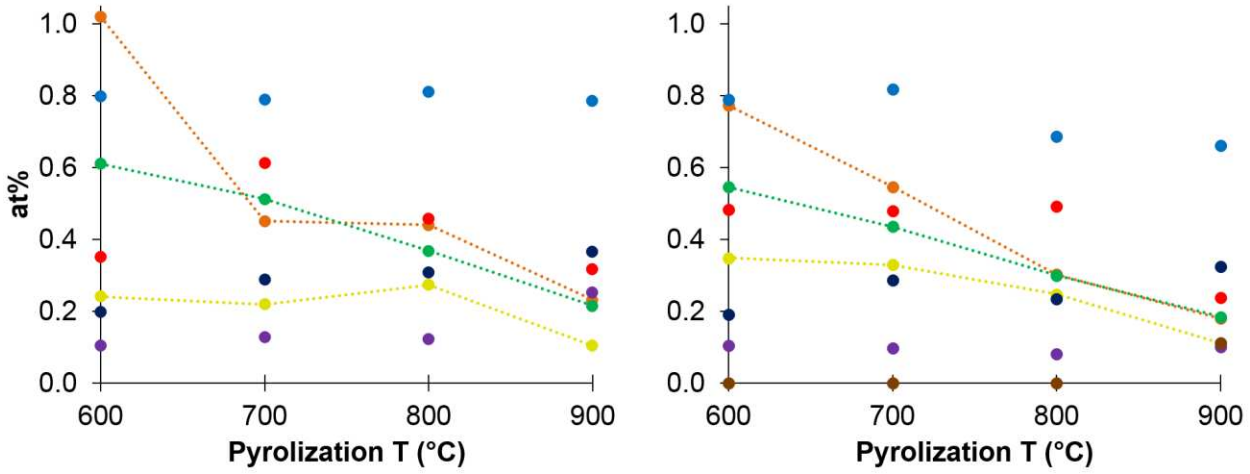

Figure 2.5 Changes in N at% and at% of N species of N-CS made with 1.18 (left) and 1.31 vol% EDA (right). Component at% correspond to binding energies of 397.2 (brown), 397.8 (red), 398.3 (orange), 399.3 (yellow), 400.1 (green), 400.8 (blue), 401.6 (indigo), and 402.5 eV (purple). Lines show the trend of pyridinic and pyrrolic species with pyrolization temperature.

2.4 Sample Preparation for Atom Probe Tomography

APT of N-CS offers potential for 3D atomic reconstructions of a single nanosphere to complement data obtained from XPS and EDS. While information obtained from XPS is surface sensitive, and includes chemical information, data is averaged over a large area of each sample (700 x 300 μm). EDS provides elemental information with nanometer resolution, but is a 2D analysis and thus cannot readily distinguish between the surface and bulk of a material. By comparison, the information that can be gained from APT is on an atomic scale and 3D, complementing information obtained with EDS and XPS.

Analysis of carbon based materials with APT has not yet been demonstrated, and before APT could be perfomed on carbon-based materials to demonstrate the technique's viability, an appropriate procedure for preparation of sample specimens must be developed. This section describes such a method for preparation of N-CS specimens for future APT analysis.

APT is typically performed on a tip about 250 nm in length and 150 nm in diameter that has been sectioned from the sample of interest via focused-ion beam scanning electron microscope

(FIB/SEM). Since the 1.18 vol% EDA N-CS being analyzed are 150-250 nm in diameter, the N-CS must first be immobilized in a stationary medium to facilitate preparation of the APT post. The medium must be devoid of C, O, and N since the 3D reconstruction of the post details elemental composition at each pixel in the post, causing differentiation between the post and the medium to be non-trivial.

To distinguish between the medium and N-CS, initial sample preparation consisted of dropcasting a solution of N-CS in ethanol onto a Si wafer, drying in an oven, and sputtering with Cu – the transition from Cu to C, O, and N in the 3D reconstruction would delineate the surface of the N-CS particle. However, the evaporation field of Cu is much lower than that of C, which caused the Cu medium to evaporate more readily than the N-CS resulting in loss of the sample during analysis. New APT samples shown in Figure 2.6A were prepared by sputtering with Au since its evaporation field was higher than Cu and thus more similar to that of C. Posts prepared from these samples still resulted in loss of the N-CS inside the atom probe due to the gaps present between N-CS particles – the N-CS were deposited as agglomerated clusters on top of the Si wafer, so sputtering with Au trapped residual atmosphere which then expanded during APT and caused the N-CS to detach from the post. Additionally, low concentration of N-CS on the surface of the wafer resulted in many posts containing no N-CS, vastly increasing preparation time on the FIB. Thus, revisions were made to the APT sample preparation procedure to both increase concentration and decrease agglomeration, resulting in clusters of N-CS a single layer thick instead of multi-layer agglomerates. Diluting the N-CS solution and increasing the RPM of the wafer during spincoating improved dispersion, while spincoating and sputtering multiple N-CS and Au layers onto the same Si wafer improved concentration as shown in Figure 2.6B. The solvent used to disperse N-CS was varied between different ratios of ethanol and dimethylformamide, but did not significantly impact

dispersion as shown in Figure 2.6C. Addition of polyvinylpyrrolidone (PVP), a surfactant, to the N-CS significantly improved dispersion as shown in Figure 2.6D, but its presence also greatly increased the apparent N at% of the sample – APT reconstructions of identical N-CS, one prepared with PVP and one without, differed by nearly 5 N at%. The conditions which resulted in greatest concentration and best dispersion of N-CS on the Si wafer were applied for all APT samples and are briefly described here.

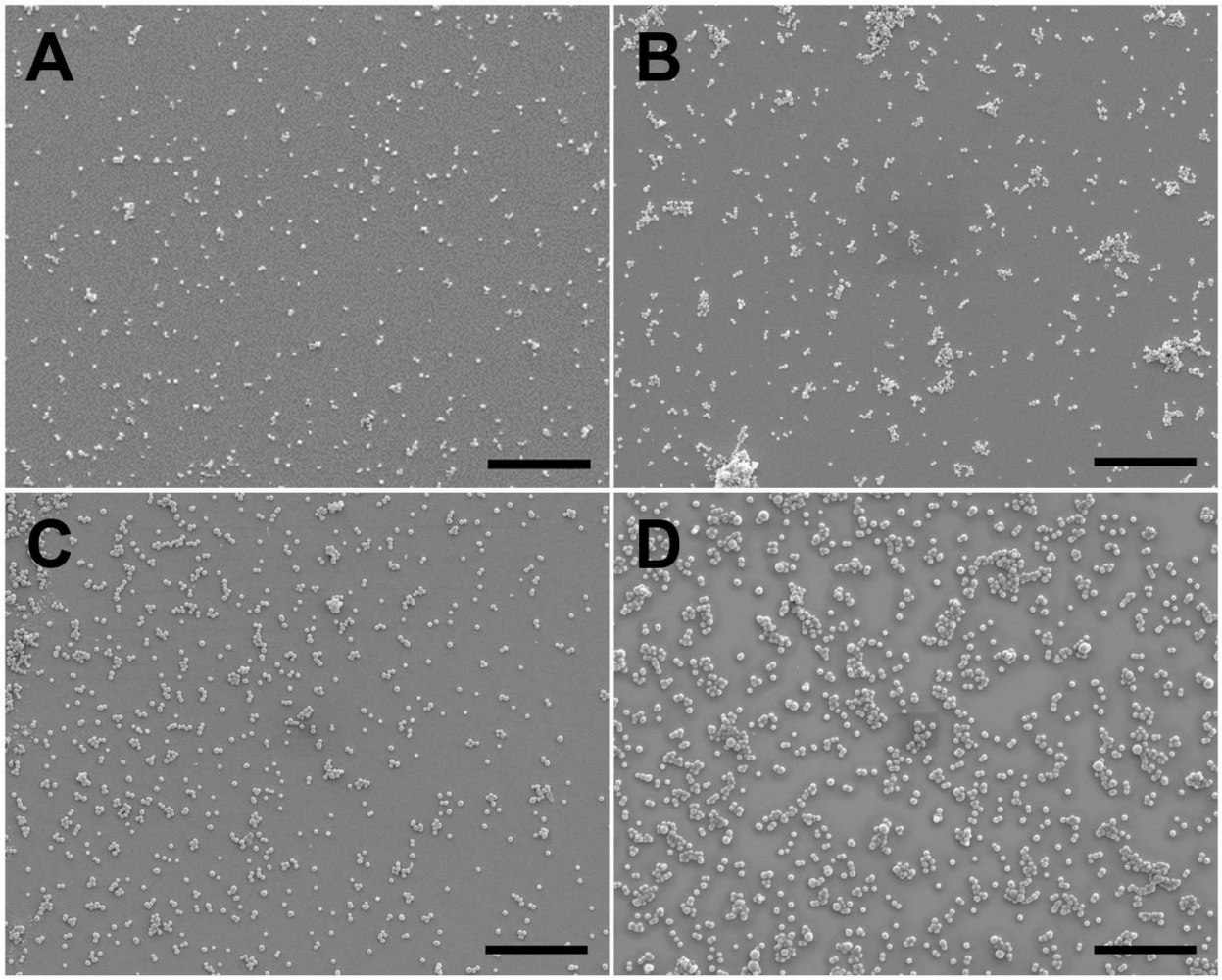

Figure 2.6 SEM of APT sample wafers prepared under various conditions. A) Si wafer dropcast with N-CS. B) Si wafer spincoated with N-CS and sputtered with Au per layer, with three layers. C) Si wafer spincoated with N-CS in 1:1 ethanol:DMF solvent. D) Si wafer spincoated with N-CS in PVP solution. Scalebars are 5 μm.

First, 1.18 vol% EDA N-CS were dispersed in ethanol to obtain a 0.4 mg/mL stock solution from which a 1 mL aliquot was further diluted to yield a 0.2 mg/mL sample solution. A clean Si wafer was then sputtered in a Hummer VI sputtering system for 12 minutes to apply a layer of Au 100 nm thick. To disperse N-CS across the surface of the wafer in single-layer clusters, a 5 μL aliquot of solution was dropped on the wafer which was then spun at 2000 RPM for 4 minutes. An additional aliquot was dropped and spincoated, then the wafer was sputtered with Au to immobilize the coated N-CS. The wafer was sputtered for 80 seconds at a 45° angle, then rotated 180° and sputtered again to prevent formation of air pockets between the N-CS and the wafer. Finally, the sequence of spin-coating and sputtering was repeated twice more to obtain a wafer coated with three alternating layers of N-CS and Au. Wafers were imaged under SEM to evaluate dispersion of N-CS across the surface of the wafer as shown in Figure 2.7, with a scratch in the surface applied to allow orientation of the images.

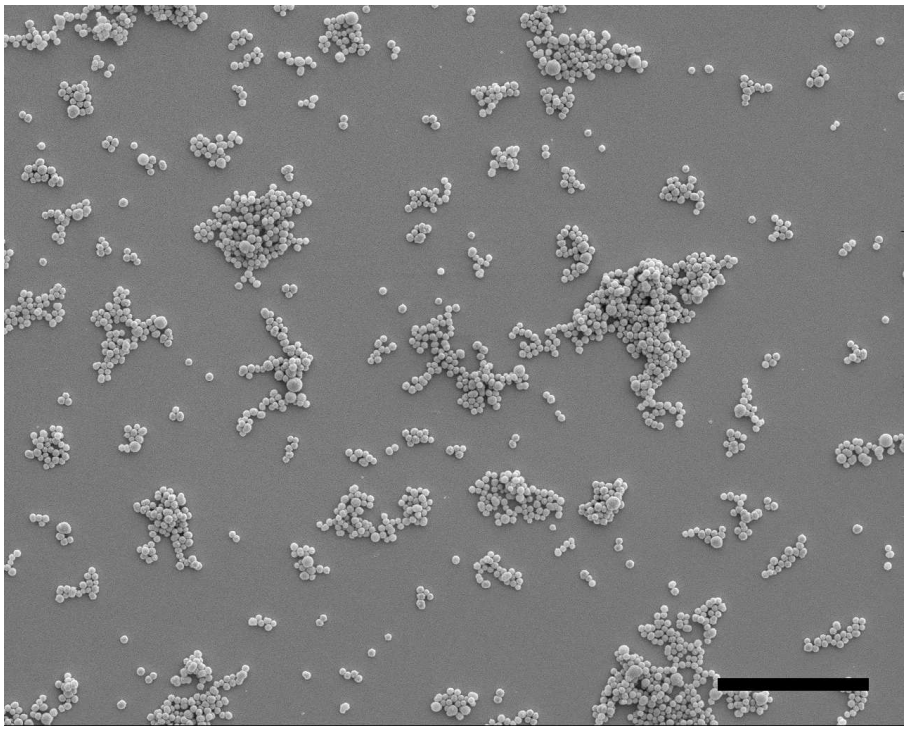

Figure 2.7 SEM of N-CS coated on an Si wafer and sputtered with Au. Clusters of N-CS that are a single layer thick were obtained. Scalebar is 5 μm.

Prior to conducting APT, EDS was used to evaluate whether an APT post contained an N-CS as shown in Figure 2.8. The C, N, and O of the sphere can be readily distinguished from the sputtered Cu and the Si wafer on which the particle was immobilized. Preliminary reconstructions of 1.18 vol% EDA N-CS run on APT show N is dispersed throughout a section of the particle as seen in Figure 2.9, but lack of an Au edge prevents identification of the surface of the particle. The N-CS diameter of 150-250 nm results in a conical section of material, rather than the entire particle, being embedded in the APT post. While the techniques developed here for analysis of N-CS materials can still be improved, the preliminary results show that analysis of carbon-based materials by APT is feasible and can provide useful insight on dispersion of N dopants throughout N-CS.

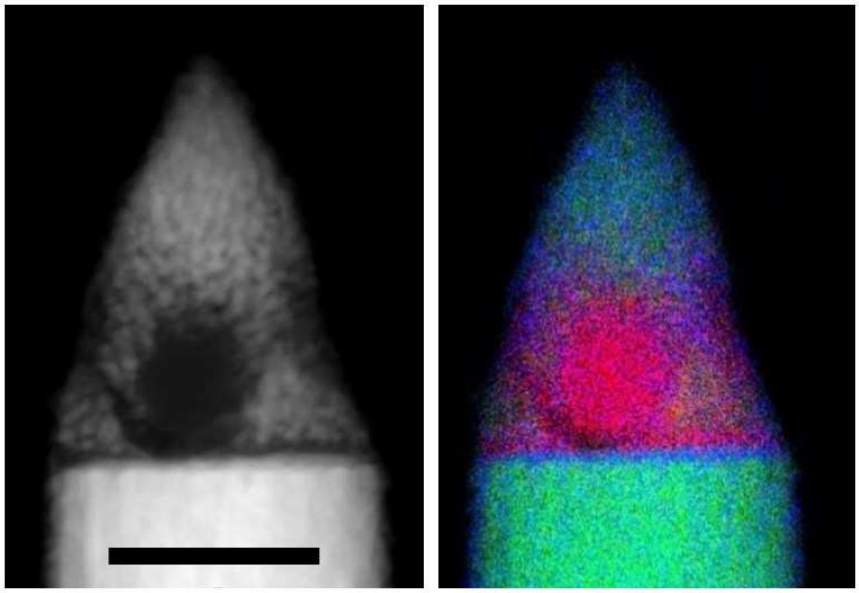

Figure 2.8 HAADF (left) and EDS elemental mapping (right) of APT post prepared with 1.31 vol% EDA N-CS sputtered with Cu. C (red), O (blue), and Cu + Si (green) show the N-CS mounted at the tip of the post. Scalebar is 100 nm.

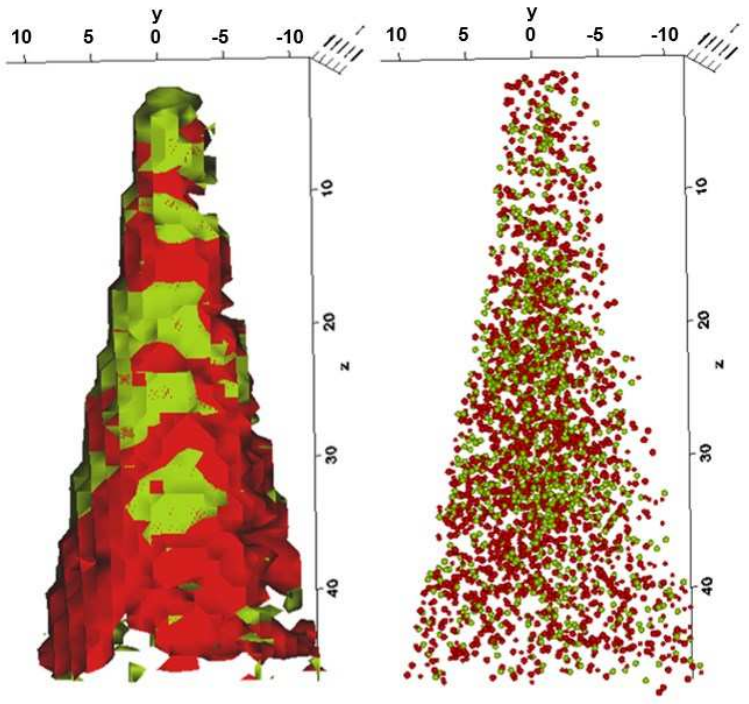

Figure 2.9 APT reconstructions of post prepared with 1.18 vol% EDA N-CS sputtered with Au. N (green) is dispersed throughout the C (red) of the material. Au, which would indicate the surface of the N-CS, is not visible.

2.5 Conclusions

To elucidate understanding of the role of N in N-doped PGM and PGM-free catalysts, a series of high-surface area model substrates with varied compositions were developed. Morphology and composition control of N-CS was achieved by adjusting EDA concentration and pyrolization temperature of the synthesis. Scale-up of synthesis increased quantity of material produced, allowing multi-technique characterization methods to be performed. A method for immobilizing N-CS to facilitate sample preparation for APT was demonstrated, and preliminary APT reconstructions show the practicality of the technique for further analysis of these materials.

CHAPTER 3

DEVELOPMENT OF MODEL FE-N-C CATALYSTS WITH CONTROLLED SHAPE AND COMPOSITION

3.1 Introduction

Chapter 3 focuses on development of model Pt group metal (PGM)-free catalysts based on iron, nitrogen and carbon (Fe-N-C) with the goal to investigate the roles of nitrogen and iron in these materials. Development of PGM-free catalysts is motivated by high cost and limited availability of platinum-based catalysts. In particular, atomically dispersed Fe has been shown to exhibit activity for the ORR.[21,23,26,28] However, current high-performing Fe-N-C materials are highly heterogeneous, making identification of active catalytic sites a challenge. The development of a series of Fe-N-C materials can therefore provide model materials for a variety of characterization methods, thereby elucidating the role of chemical species of interest.

This work extends application of the solvothermal treatment used to synthesize N-CS resins for fabrication of a series of Fe-N-C materials with the goal to produce atomically dispersed Fe species coordinated with nitrogen. Fe-N-C materials were prepared via addition of an Fe precursor prior to the solvothermal treatment used to synthesize N-CS resins. A variety of Fe precursors were utilized to elucidate the effect of Fe cation valency, ligands, and presence of N in ligands on loading and dispersion of Fe: iron (II) chloride ($FeCl_2$), iron (II) acetate ($Fe(acet)_2$), iron tris-ethylenediamine (II) chloride ($Fe[EDA]_3Cl_2$), iron (III) acetylacetonate ($Fe(acac)_3$), and iron (III) chloride hexahydrate ($FeCl_3 \cdot 6\ H_2O$). Initially all Fe-N-C materials were prepared with 1.18 vol% EDA and pyrolysis temperature of 600 °C. Thermogravimetric analysis (TGA) was used to obtain decomposition profiles of unpyrolized Fe-N-C to determine which additional pyrolization temperatures should be used for each material.

3.2 Solvothermal Synthesis of Fe-N-C

Preparation of Fe-N-C samples was performed by modifying the synthesis of N-CS previously described in Chapter 2 via addition of an Fe precursor prior to addition of resorcinol. A 2 L batch size and 1.18 vol% EDA were selected, and all other synthesis parameters were unchanged. A theoretical 5 wt% Fe loading was selected for all samples since Fe-N-C with similar weight loadings have been reported in the literature, equivalent to 46.3 mg Fe for a 880 mg yield of N-CS as calculated by Equation 3.1:

$$m_{Fe} = m_{N-CS} \cdot \frac{wt\%_{Fe}}{1-wt\%_{Fe}} \tag{3.1}$$

where m_{Fe} is the mass of Fe present, $m_{N\text{-}CS}$ is the mass of N-CS obtained from one 2 L batch, and $wt\%_{Fe}$ is the theoretical wt% of Fe. The mass of each Fe precursor that was added to obtain 46.3 mg Fe is calculated from the molecular weight of the precursor and is shown in Table 3.1. Throughout this chapter, Fe-N-C materials are referred to by the nomenclature [precursor]-NC-X00, where [precursor] refers to the Fe precursor used to prepare that sample and X00 is the pyrolization temperature used.

Table 3.1 Calculation of mass of each Fe precursor added to obtain 46.3 mg of Fe, which corresponds to a theoretical 5 wt% loading of Fe in Fe-N-C.

Fe precursor	MW (g/mol)	Mass added (g)
$FeCl_2$	126.75	105.1
$Fe(acet)_2$	173.93	144.2
$Fe[EDA]_3Cl_2$	307.05	254.6
$FeCl_3 \cdot 6\ H_2O$	270.29	224.1
$Fe(acac)_3$	353.17	292.8

Decomposition profiles of unpyrolyzed Fe-N-C were obtained for each Fe precursor under flowing nitrogen and are shown in Figure 3.1. A clean Pt pan was tared on a TA Q500 TGA instrument, then 2-3 mg of unpyrolyzed material was placed in the pan. Sample and balance gas flow rates were set to 20 and 40 mL/min respectively, and a heating ramp of 5 °C/min up to

1000 °C was selected. Another set of Fe-N-C prepared by addition of Fe precursor to N-CS following pyrolization was prepared and run on TGA as well, and is shown for comparison.

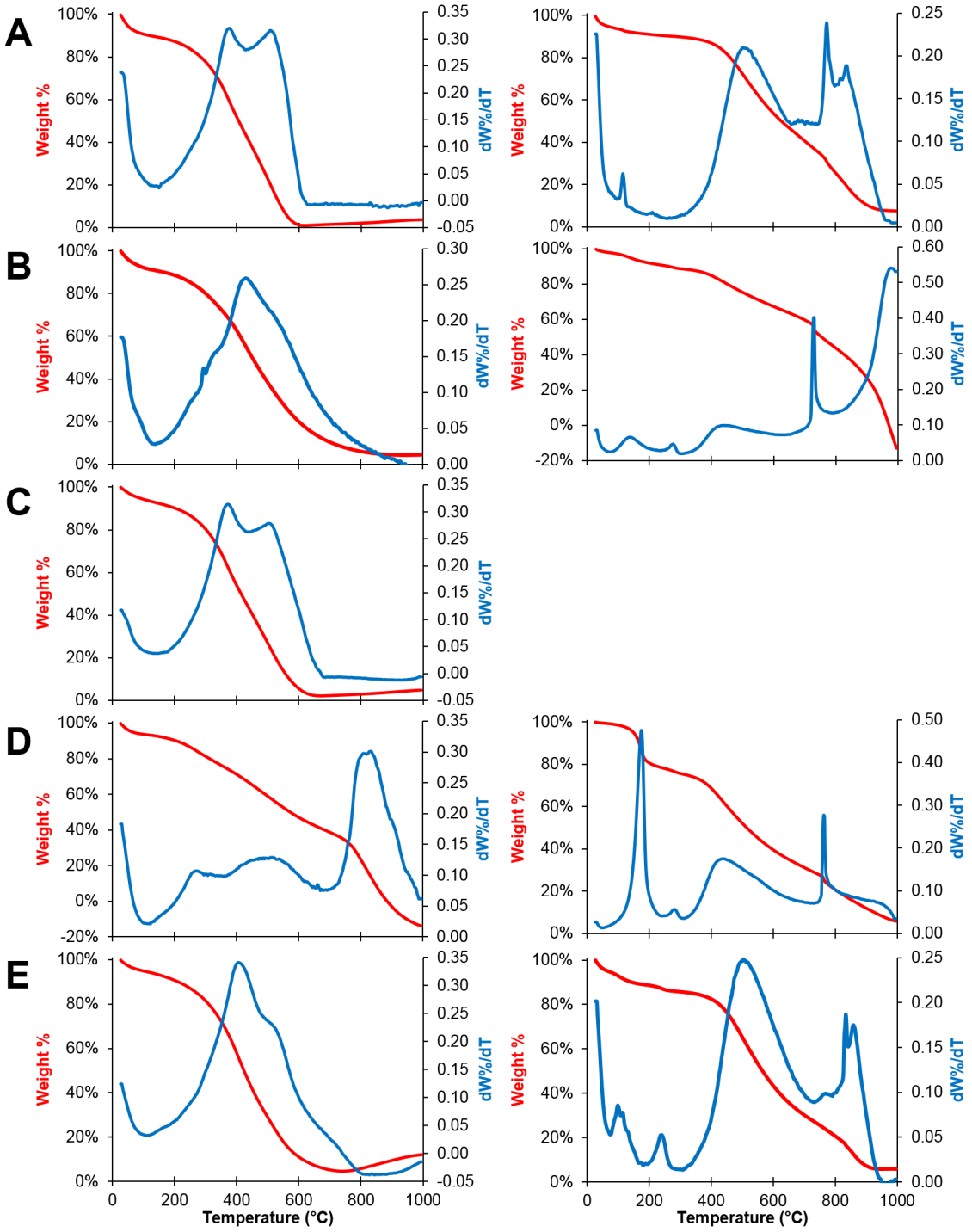

Figure 3.1 TGA of Fe-N-C prepared via addition of Fe precursor prior to solvothermal treatment (left) and after pyrolization of N-CS (right). Profiles correspond to Fe precursors of $FeCl_2$ (A), $Fe(acet)_2$ (B), $Fe[EDA]_3Cl_2$ (C), $Fe(acac)_3$ (D), and $FeCl_3 \cdot 6\ H_2O$ (E).

Most Fe-N-C prepared via addition of Fe precursor prior to solvothermal treatment underwent decomposition below 600 °C, except for the $Fe(acac)_3$ sample which decomposed in the 800-900 °C range. This temperature range was used as a guide for further synthesis: additional Fe-N-C were prepared using each Fe precursor, and were pyrolzed at 700, 800, and 900 °C.

3.3 Physiochemical Characterization

Fe-N-C samples were analyzed by TEM and XPS using the same methods described in Chapter 2 for N-CS samples. Select samples were further analyzed by EDS to observe dispersion of Fe, as well as Mossbauer spectroscopy (not reported here), a technique useful for both identifying Fe species present and quantifying their relative amounts.

3.3.1 TEM

The particle sizes in all Fe-N-C samples increased by roughly 20% compared to the N-CS samples prepared at the same vol% EDA and pyrolization temperature as shown in Figure 3.2, with 250-300 nm spheres as well as infrequent 400-500 nm spheres. In addition to the discrete spherical nanoparticles, some of the material was present as finer particles with no specific shape. Qualitatively, $Fe(acet)_2$-NC tended to have the least proportion of these disordered (in terms of shape not necessarily structure) particles, while $FeCl_3 \cdot 6\ H_2O$-NC had the most.

Previous work indicates that PGM-free catalysts such as Fe have greater activity when atomically dispersed in a supporting material rather than as discrete nanoparticles;[21,29] the presence of Fe nanoparticles can be detrimental to activity due to crossover during cycling. Thus, it is important to determine the relative distribution of Fe between Fe nanoparticles and atomically dispersed Fe species. From initial evaluation of low magnification TEM images, the amount of Fe present as nanoparticles can be assessed. In general, Fe nanoparticles were not observed in Fe-N-C pyrolyzed at 600 °C, while 10-20 nm Fe nanoparticles were present in Fe-N-C samples

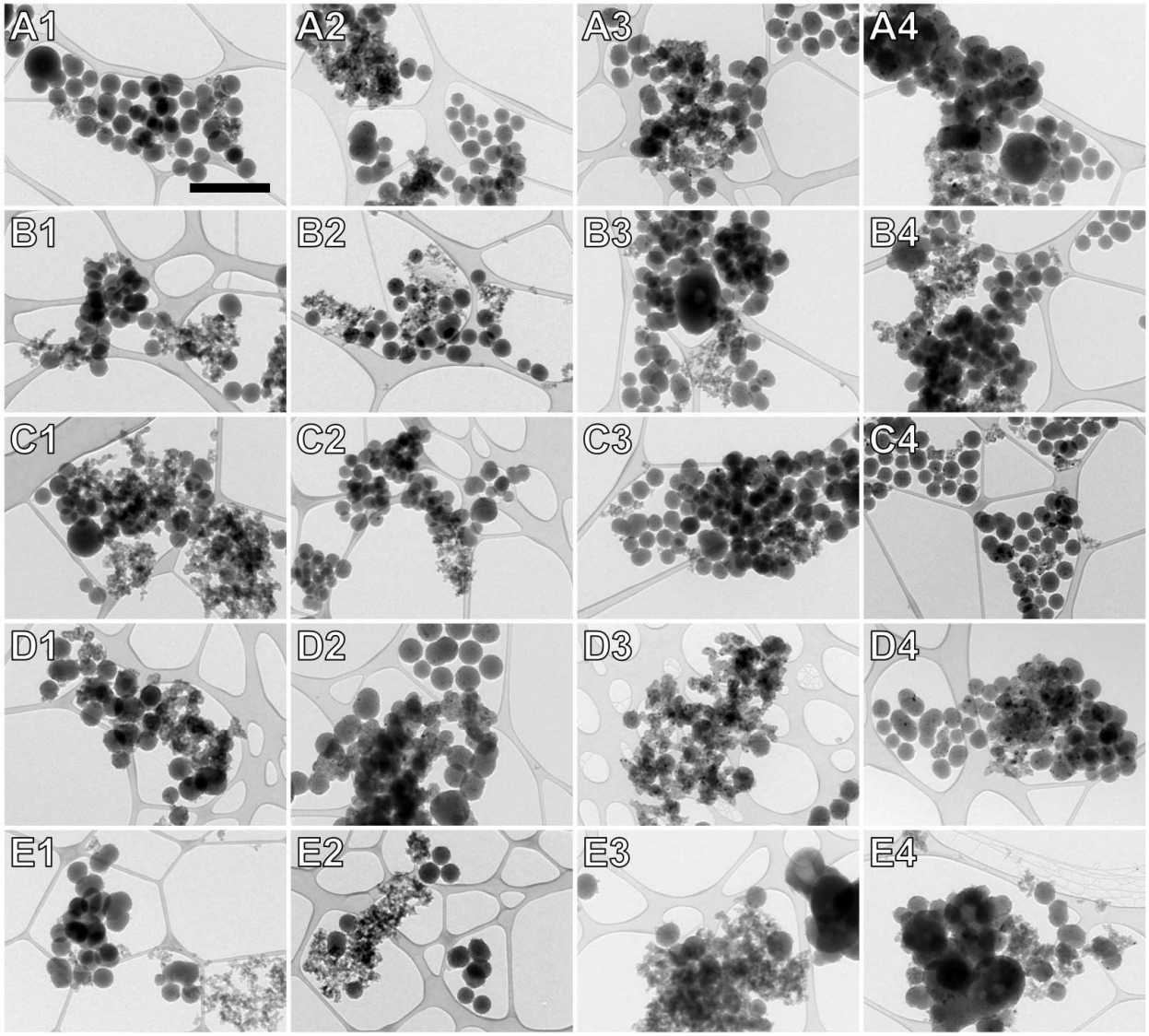

Figure 3.2 TEM of Fe-N-C samples prepared with a variety of Fe precursors and pyrolyzed at 600 (1), 700 (2), 800 (3), or 900 (4) °C. Images correspond to Fe precursors as follows: $FeCl_2$ (A), $Fe(acet)_2$ (B), $Fe[EDA]_3Cl_2$ (C), $Fe(acac)_3$ (D), and $FeCl_3 \cdot 6\ H_2O$ (E). Scalebar is 1 μm and all images were taken at the same magnification.

pyrolyzed at 700 °C or greater. Exceptions existed for $Fe(acet)_2$-NC-600, which yielded infrequent 10-20 nm Fe nanoparticles, and for $FeCl_3 \cdot 6\ H_2O$-NC-700, which did not yield Fe nanoparticles.Of the Fe-N-C prepared, $Fe(acet)_2$-NC tended to yield the greatest number of Fe nanoparticles while $FeCl_3 \cdot 6\ H_2O$-NC yielded the least as shown in Figure 3.3. Size of Fe nanoparticles did not significantly vary with pyrolization temperature; instead the frequency of Fe nanoparticles was qualitatively seen to increase as pyrolization temperature increased.

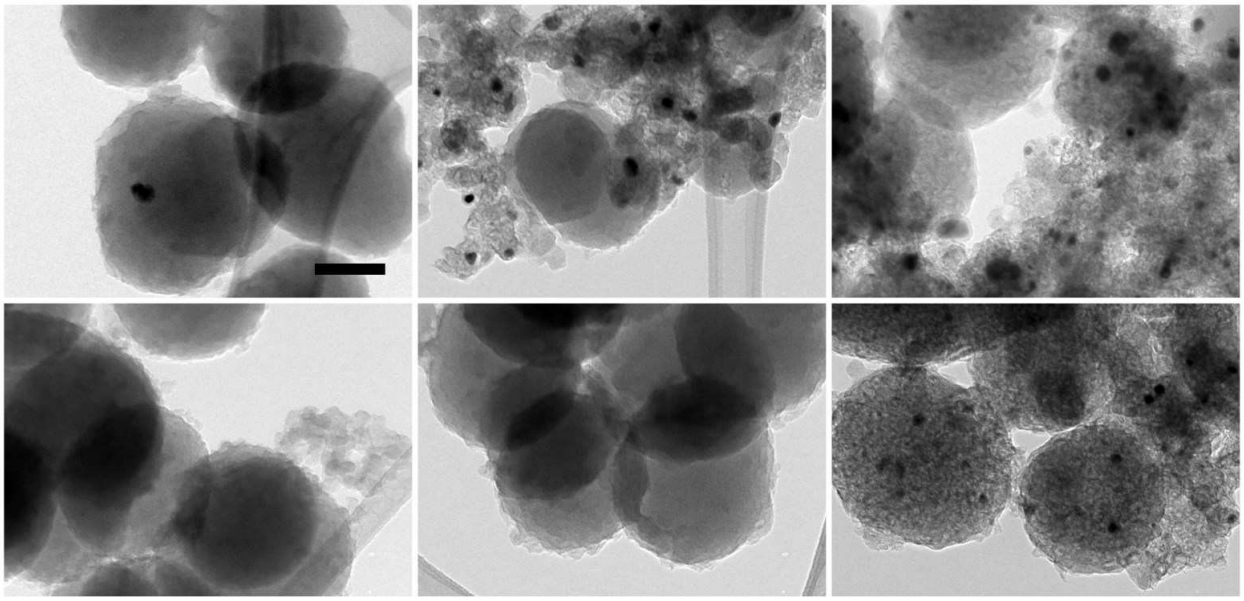

Figure 3.3 TEM of Fe-N-C showing presence of Fe nanoparticles. Samples were pyrolyzed at 600 (left), 700 (middle), or 900 (right) °C, and used Fe precursors of $Fe(acet)_2$ (top) or $FeCl_3 \cdot 6\ H_2O$ (bottom). Scalebar is 100 nm and all images were taken at the same magnification.

Since activity of a catalyst can be improved by increasing the number of active sites, increasing the Fe loading can result in a material that is more catalytically active. However, attempts to increase Fe at% by increasing concentration of Fe precursor resulted in heavily agglomerated material that did not maintain spherical morphology as shown in Figure 3.4. Additonally, Fe nanoparticles of 15-30 nm size with occasional 100-125 nm particles were present on the 10 wt% Fe-N-C, in contrast to the 5 wt% Fe-N-C on which no particles could be seen. The goal of increasing Fe loading was to incorporate more atomic Fe while preserving shape; since shape was lost, this synthesis was not pursued further. Since it has been previously reported that Fe-N-C materials are most active when prepared at 0.2-4 wt% nominal loading,[23,29] Fe-N-C with $Fe(acet)_2$ was also prepared at 4 wt% Fe. As shown in Figure 3.5, the 4 wt% Fe material contained fewer Fe nanoparticles than the 5 wt% Fe. Additionally, polydispersity of the sample was improved as fewer 400-500 nm spheres and a lower amount of disordered material was present.

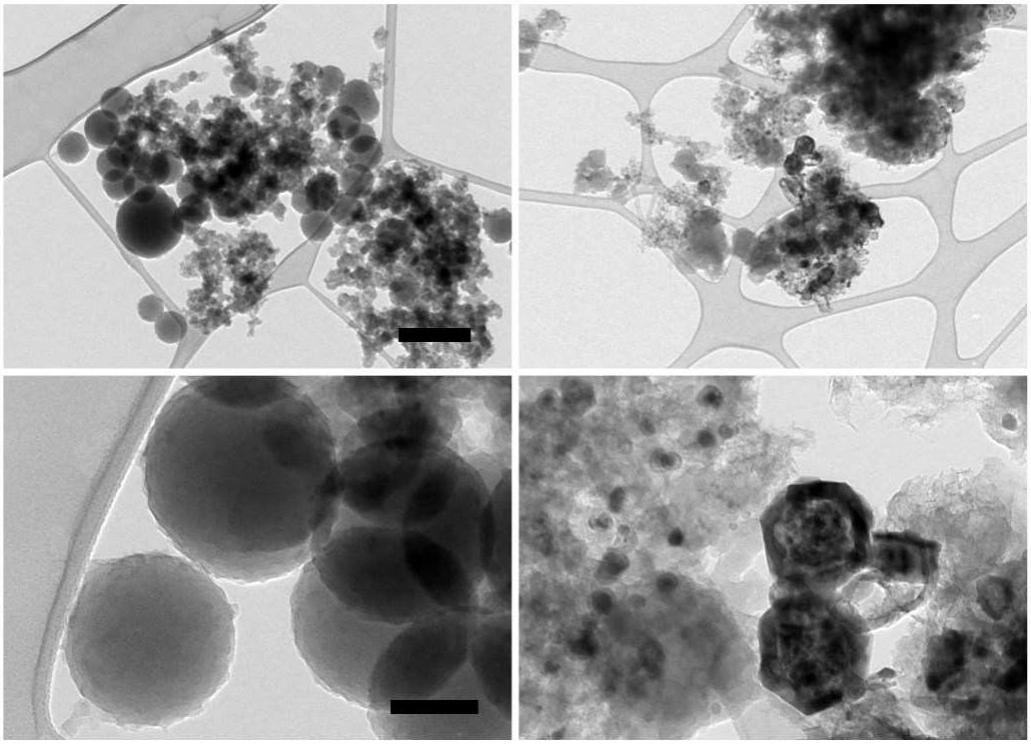

Figure 3.4 TEM comparison of 5 (left) and 10 (right) wt% Fe-N-C samples prepared with $Fe[EDA]_3Cl_2$ at 600 °C. Scalebars are 500 nm (top) and 100 nm (bottom).

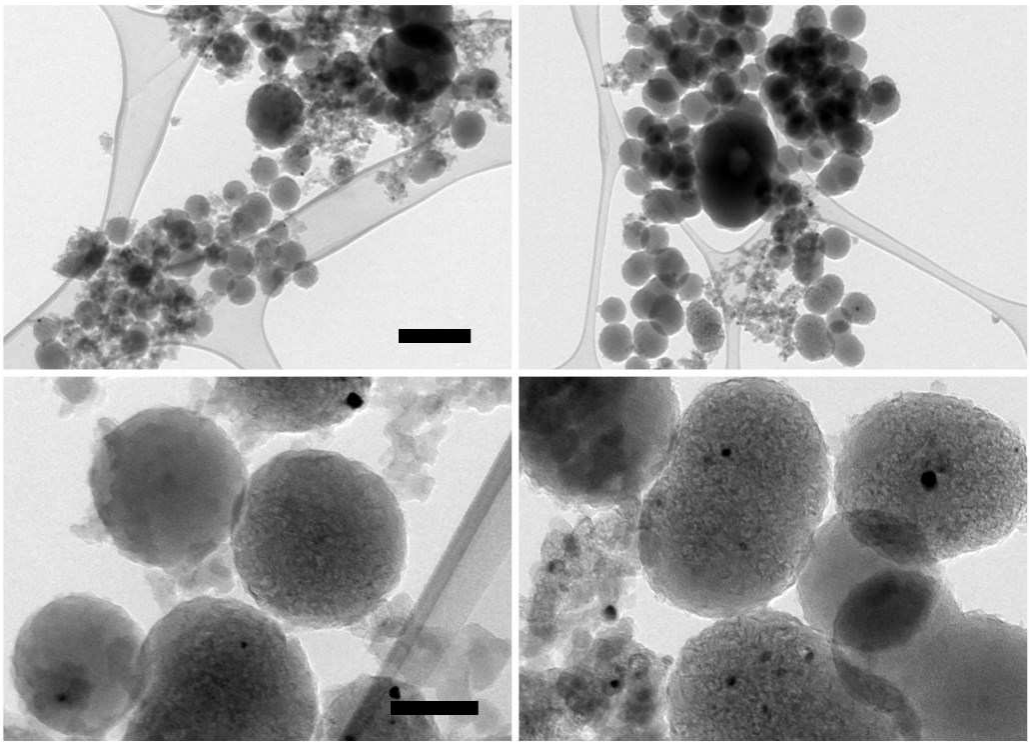

Figure 3.5 TEM comparison of 4 (left) and 5 (right) wt% Fe-N-C samples prepared with $Fe(acet)_2$ at 800 °C. Scalebars are 500 nm (top) and 100 nm (bottom).

Several Fe-N-C were selected for further characterization by EDS and XPS based on features seen in TEM. $Fe(acet)_2$-NC exhibited the greatest frequency of Fe nanoparticles, while $FeCl_3 \cdot 6\ H_2O$-NC possessed the least.

3.3.2 EDS

Since atomically dispersed Fe is catalytically active but cannot be observed via TEM, elemental mapping via EDS can be used to determine distribution of Fe throughout the material. Elemental maps of N and Fe for both $Fe(acet)_2$-NC-600 and $FeCl_3 \cdot 6\ H_2O$-NC-600 are shown in Figure 3.6, showing good dispersion of Fe throughout both spherical and non-spherical particles. Fe on $FeCl_3 \cdot 6\ H_2O$-NC-600 is slightly more well-dispersed than that of $Fe(acet)_2$-NC-600, as Fe can be seen separate fom N in the N+Fe map of the latter. Actual Fe loading on these Fe-N-C is significantly lower than the nominal 5 wt% loading as shown in Table 3.2, indicating that not all Fe from the Fe precursors was incorporated into the N-CS during synthesis. Fe loading on $Fe(acet)_2$-NC-600 was slightly higher, which could contribute to the increased frequency of Fe nanoparticles seen in $Fe(acet)_2$-NC relative to other Fe-N-C and suggests uptake of $Fe(acet)_2$ by N-CS during synthesis is more favorable than the uptake from $FeCl_3 \cdot 6\ H_2O$-NC-600. Trace at% of Cu, Si, and Cl occur primarily from the Cu grid and backing on which the Fe-N-C were mounted. Elemental maps of $FeCl_3 \cdot 6\ H_2O$-NC-700 were also acquired to investigate the effect of pyrolization temperature on Fe dispersion and loading. An increase in non-dispersed Fe is seen, which correlates with the increase in Fe wt% seen in Table 3.2 and the qualitative increase in Fe nanoparticle count seen with increasing pyrolization temperature.

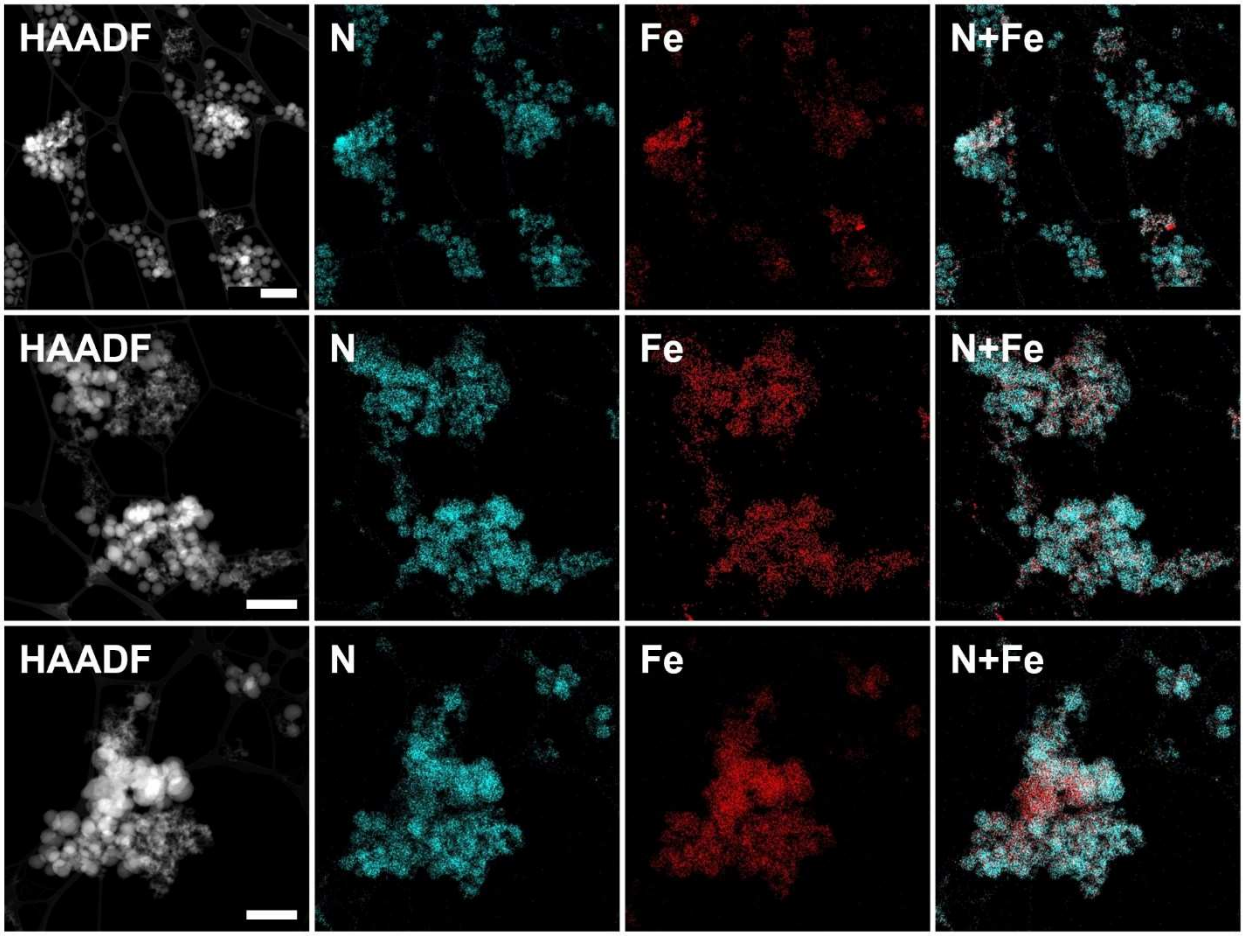

Figure 3.6 EDS elemental mapping of Fe-N-C pyrolyzed at 600 °C. Samples were prepared with $Fe(acet)_2$ (top) or $FeCl_3 \cdot 6\ H_2O$ (bottom). Scalebars are 1 μm, and all images on the same row were taken at the same magnification.

Table 3.2 Elemental compositions of $Fe(acet)_2$-NC-600 and $FeCl_3 \cdot 6\ H_2O$-NC-600.

Element	**$Fe(acet)_2$-NC-600**		**$FeCl_3 \cdot 6\ H_2O$-NC-600**		**$FeCl_3 \cdot 6\ H_2O$-NC-700**	
	wt%	**at%**	**wt%**	**at%**	**wt%**	**at%**
C	90.7	93.5	90.1	94.2	90.15	94.8
N	4.4	3.9	2.8	2.6	2.64	2.4
O	2.7	2.1	3.1	2.4	2.28	1.8
Fe	1.1	0.2	0.8	0.2	1.26	0.3
Cu	1.0	0.2	3.0	0.6	3.60	0.7
Cl	0.06	0.03	0.05	0.02	0.04	0.01
Si	0.01	0.02	0.04	0.02	0.03	0.02

3.3.3 XPS

High-resolution XPS spectra of C 1s, O 1s, N 1s, and Fe 2p were analyzed with CasaXPS with the same methods described in Chapter 2. All samples were mounted on conductive tape so were not calibrated, and Fe 2p spectra were fit with a Shirley instead of a linear background. Differences between the at% obtained from EDS and XPS as shown in Table 3.3 are indicative of composition changes between the surface and bulk of the Fe-N-C. Specifically, the surface of $Fe(acet)_2$-NC-600 had lower N at% while both $FeCl_3 \cdot 6\ H_2O$-NC had increased N at%. All samples had increased O at% and decreased Fe at% at their surface. The decrease in Fe at% could result from Fe being incorporated throughout N-CS spheres either atomically or as a nanoparticle, thus decreasing the at% found by XPS. Key trends seen in EDS were corroborated by the XPS data: $Fe(acet)_2$-NC-600 had increased Fe at% compared to $FeCl_3 \cdot 6\ H_2O$-NC-600 due to higher uptake of $Fe(acet)_2$ by N-CS during synthesis, and higher pyrolization temperature also resulted in increased Fe at%. Analysis of the components of the Fe 2p XPS spectra to identify which species of Fe were present could not be performed due to the high signal-to-noise ratio caused by low total Fe at% in these samples. As such, there is insufficient data to include a detailed discussion of which Fe species and N species compose the active site of these catalysts, instead X-ray absorption spectroscopy studies are planned in the future.

Table 3.3 Concentration of C, N, O, and Fe obtained from XPS and EDS of $Fe(acet)_2$-NC-600 and $FeCl_3 \cdot 6\ H_2O$-NC-600 and 700. EDS at% were normalized here to 100% from the values shown in Table 3.2.

Element	**$Fe(acet)_2$-NC-600**		**$FeCl_3 \cdot 6\ H_2O$-NC-600**		**$FeCl_3 \cdot 6\ H_2O$-NC-700**	
	EDS at%	**XPS at%**	**EDS at%**	**XPS at%**	**EDS at%**	**XPS at%**
C	93.7	87.1	94.8	86.3	95.5	91.4
N	4.0	2.8	2.6	3.2	2.4	4.1
O	2.1	9.9	2.4	10.3	1.8	4.3
Fe	0.2	0.2	0.2	0.2	0.3	0.2

3.4 Conclusions

PGM-free catalysts are a cost-effective alternative to PGM catalysts for the ORR in fuel cells, but characterization of the active site of high-performing PGM-free catalysts remains a challenge. In this work, a series of Fe-N-C with varied compositions were developed by incorporating a range of Fe precursors into N-CS materials. The Fe precursor used was found to impact both Fe loading in Fe-N-C as well as formation of non-spherical particles, and pyrolization temperature caused in increase in Fe loading and increased frequency of Fe nanoparticles in addition to atomically dispersed Fe. The development of these series of Fe-N-C materials allows for further characterization by electrochemistry and atom probe tomography to identify sites which influence performance in ORR. While correlating ORR performance with curve-fitting of N 1s XPS spectra provides valuable information, the correlations derived are based on an N 1s signal averaged over hundreds of microns, and includes all species located within 10 nm of the surface layer. The true goal of this work is to obtain an atomic-scale 3D distribution of species at the surface of an individual Fe-N-C nanosphere, enabling correlations between ORR and the species that are located at the very surface which can potentially contribute to activity.

CHAPTER 4

DEVELOPMENT OF MODEL PT/N-C MATERIALS WITH PT NANOPARTICLES

4.1 Introduction

Chapter 4 focuses on development of model catalysts incorporating Pt group metal (PGM) nanoparticles in order to investigate the role of nitrogen in activity, stability, and dispersion of these materials for the oxygen reduction reaction (ORR). Series of Pt/C and Pt/NC materials were prepared via reduction of $H_2PtCl_6 \cdot 6\ H_2O$ by $NaBH_4$ following a proprietary method not reported here, and by ethylene glycol (EG) following a previously reported method.[52] Two methods were utilized for preparation of samples since prior research indicates that the synthesis method influences interactions between PGM nanoparticles and the support material, impacting dispersion and particle size.[53] The syntheses were performed with an undoped carbon reference, Vulcan black (Cabot XC72R), and N-doped carbon supports (N-CSs) that were synthesized as described in Chapter 2 using 1.18 vol% EDA and pyrolyzing at 600 (NC-600) or 900 °C (NC-900).

4.2 Experimental

100 mg of carbon support was dispersed in 60 mL of EG (Macron Fine Chemicals, ACS grade) in a 250 mL round bottom flask, then sonicated for 15 min. 1.349 mL of aqueous 0.02 M $H_2PtCl_6 \cdot 6\ H_2O$ (Alfa Aesar, ≥99.999%) was added to the solution for a nominal 5 wt% loading of Pt, then the solution was stirred at 300 RPM for 30 min. After stirring, reaction pH was increased to 11 via dropwise addition of 5 mL of 0.04 M KOH (Macron Fine Chemicals, ACS grade). Reduction of $H_2PtCl_6 \cdot 6\ H_2O$ was achieved by connecting the round bottom flask to a reflux condenser and refluxing at 140 °C in a pre-heated mineral oil bath for 2 hr while continuing to stir at 300 RPM. The flask was then removed from heat and allowed to cool at room temperature while stirring.

Pt/C and Pt/NC was isolated from the reaction mixture by diluting the solution with 2x volume of nanopure H_2O (18.2 MΩ) and centrifuging at 9000 RPM (9327 g) in a Marathon 22kbr centrifuge. The supernatant was removed via vacuum aspiration, then re-dispersed in nanopure H_2O. Two more cycles of centrifugation, aspiration, and re-dispersion were performed to remove residual KOH and KCl from solution, then the suspension was dried in a vacuum oven at -20 in Hg and 50 °C to isolate dried Pt/C or Pt/NC.

Materials were characterized via TEM, with select materials further characterized by EDS. Characterization parameters for all methods were identical to those used in Chapter 2.

4.3 Physiochemical Characterization

4.3.1 TEM

TEM of Pt/Vulcan shows good dispersion of 2-4 nm Pt nanoparticles across the Vulcan support for both $NaBH_4$ and EG reduction methods as shown in Figure 4.1. However, the $NaBH_4$ method caused significant Pt agglomeration in Pt/NC-600, thus the EG method was selected for all further Pt/C and Pt/NC syntheses. All materials prepared via EG reduction contained 2-4 nm Pt nanoparticles dispersed across the support as shown in Figure 4.2.

4.4 Conclusions

A series of PGM catalysts based on previously developed N-CS substrates were developed to obtain materials which could be further characterized for ORR activity and catalyst composition. Reduction of $H_2PtCl_6 \cdot 6\ H_2O$ via ethylene glycol yielded well-dispersed 2-4 nm Pt nanoparticles on both N-CS and commercially available Vulcan, resulting in samples ideal for further characterization.

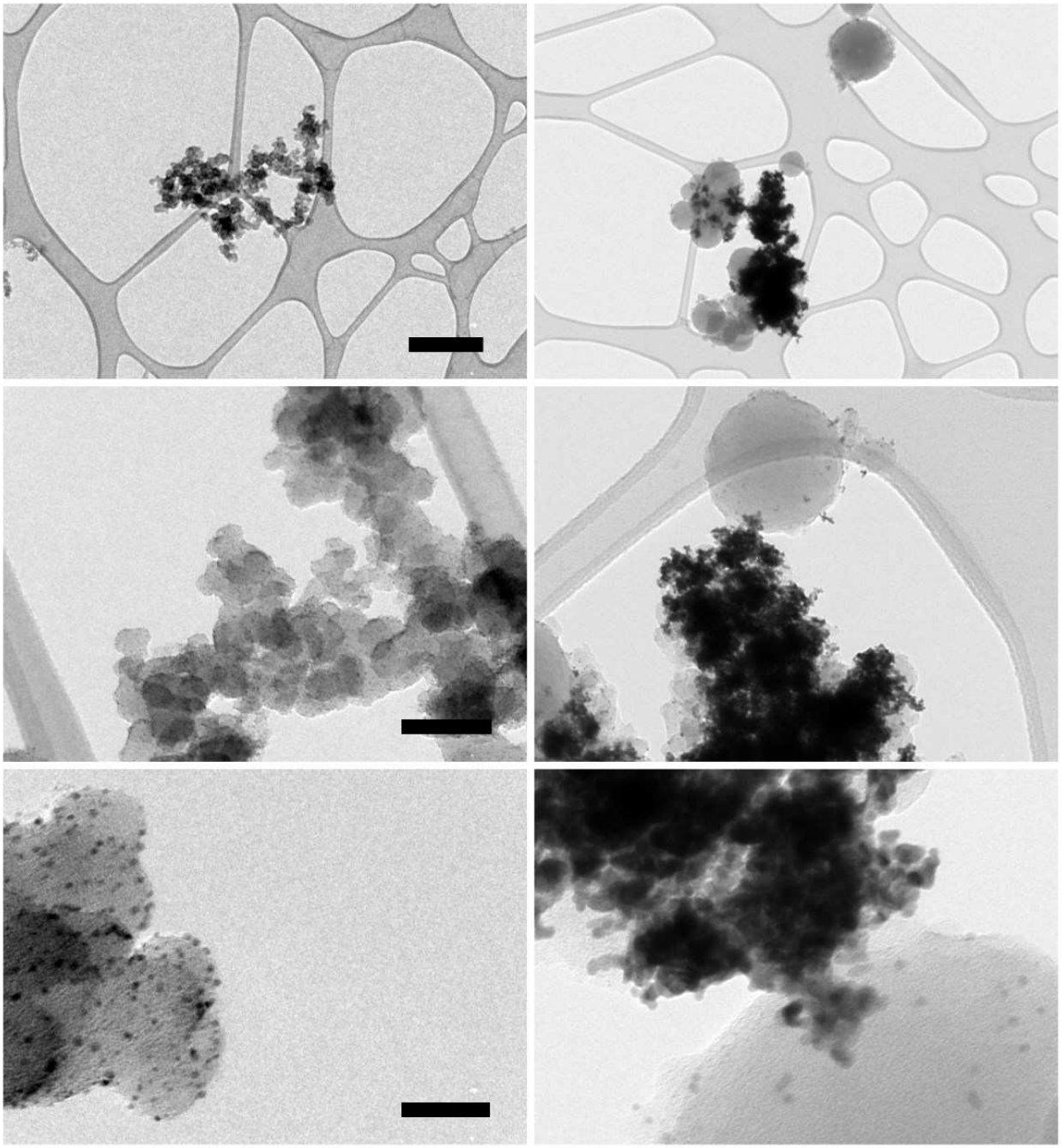

Figure 4.1 TEM of Pt/Vulcan (left) and Pt/NC-600 (right) prepared via proprietary $NaBH_4$ reduction method. Scalebars are 500 nm (top), 100 nm (middle), and 25 nm (bottom).

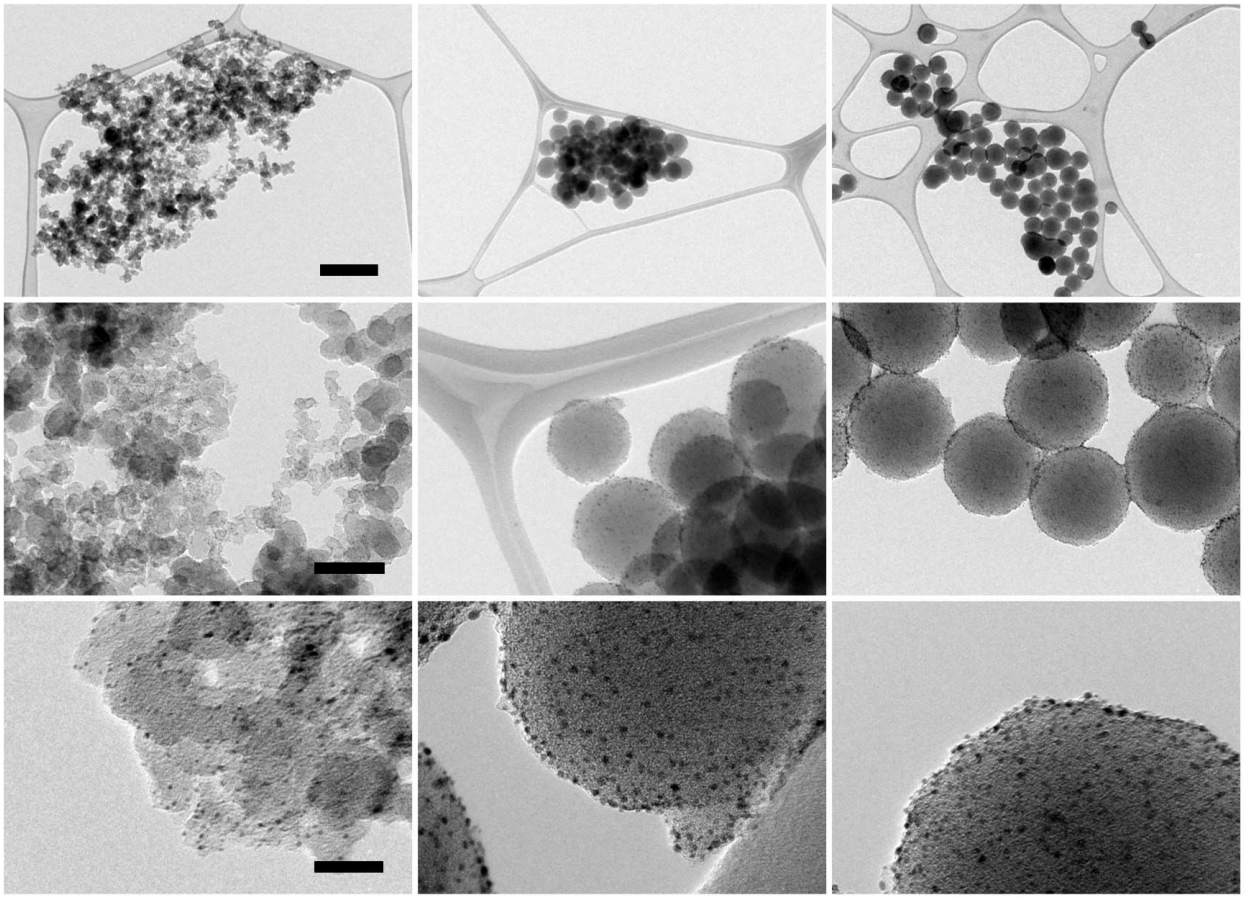

Figure 4.2 TEM of Pt/Vulcan (left), Pt/NC-600 (middle), and Pt/NC-900 (right) synthesized via reduction of $H_2PtCl_6 \cdot 6\ H_2O$ by EG. Scalebars are 500 nm (top), 100 nm (middle), and 25 nm (bottom).

CHAPTER 5

MECHANISTIC STUDY OF SHAPE-ANISOTROPIC NANOMATERIALS SYNTHESIZED VIA SPONTANEOUS GALVANIC DISPLACEMENT

A paper published in The Journal of Physical Chemistry C, reprinted with permission from DOI: 10.1021/acs.jpcc.6b07363 (article) *J. Phys. Chem. C* **2016**, *120*, 25053-25060.

Matthew B Strand,[⊥] G. Jeremy Leong,[⊥] Christopher J. Tassone, Brian Larsen, K. C. Neyerlin, Brian Gorman, David R. Diercks, Svitlana Pylypenko, Bryan Pivovar, and Ryan M. Richards*

5.1 Abstract

Among the broad portfolio of preparations for nanoscale materials, spontaneous galvanic displacement (SGD) is emerging as an important technology because it is capable of creating functional nanomaterials that cannot be obtained through other routes and may be used to thrift precious metals used in a broad range of applications including catalysis. With advances resulting from increased understanding of the SGD process, materials that significantly improve efficiency and potentially enable widespread adoption of next generation technologies can be synthesized. In this work, PtAg nanotubes synthesized via displacement of Ag nanowires by Pt were used as a model system to elucidate the fundamental mechanisms of SGD. Characterization by X-ray diffraction (XRD), small-angle X-ray scattering (SAXS), and atom probe tomography (APT) indicates nanotubes are formed as Ag is oxidized first from the surface and then from the center of the nanowire, with Pt deposition forming a rough, heterogeneous surface on the PtAg nanotube.

5.2 Introduction

Development of improved nanoscale materials requires greater control of matter at the nanoscale, and spontaneous galvanic displacement (SGD) reactions are one of the promising technologies that offer this capability. SGD consists of the processes of corrosion and electrodeposition occurring concurrently: template nanoparticles composed of less noble metal atoms act as a reducing agent for more noble metal ions in solution,[54] where the nobility of metals under standard conditions is defined by standard reduction potentials (E^0). The less noble metal is corroded as its electrons reduce the more noble metal ions in solution; Ag^0 atoms in a Ag template nanoparticle are oxidized to Ag^+ as more noble metal cations Pt^{2+} are reduced and deposited as Pt^0 on the template.[55] One of the earliest examples of SGD was reported 1970 when Turkevich and Kim synthesized Au−Pd core−shell nanoparticles by displacing the surface of Pd nanoparticles with $HAuCl_4$.[56] In this way, SGD can be applied to nanomaterials and has already demonstrated value in electrocatalysis for fuel cells.[5,57–60] The conversion of Ag nanoplates to Pt nanoplates is shown in Figure 5.1 as an illustrative example: $2Ag + PtCl_4^{2-} \rightarrow 2AgCl + 2Cl^- + Pt^0$.

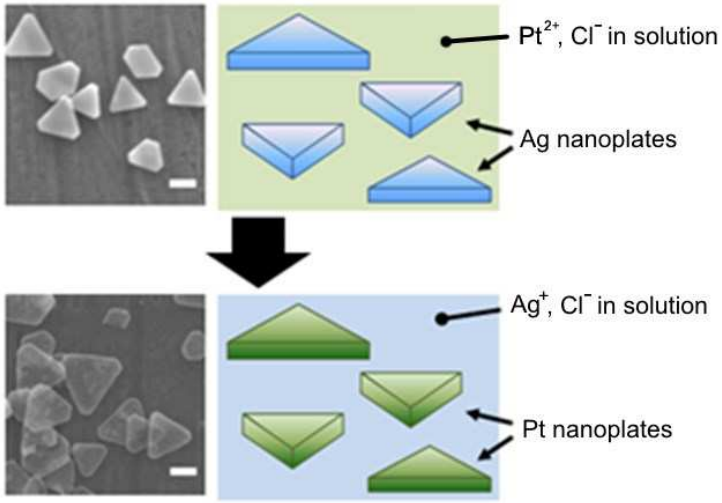

Figure 5.1 Ag nanoplates (top) may be used as displacement templates in SGD reactions to synthesize Pt nanoplates (bottom) (ref 58).

SGD can be used to synthesize a variety of functional nanomaterials that cannot necessarily be produced by other methods with examples such as Pt nanotubes from Ag nanowires[61] or structures/compositions such as bimetallic[55,57,62–68] or trimetallic materials.[69,70] It also has the potential to create high surface area porous nanostructures,[71–73] thrift high-cost materials, for example, by using a Ni nanoparticle template to deposit an ultrathin layer of Pt/Au,[70] and the ability to tune structures through the use of surfactants, metal ion size, crystal structure, or metal ion valency.[74] It is thus possible to synthesize shape-controlled nanomaterials by SGD reactions with a degree of compositional control that cannot be otherwise obtained. Elucidation of the displacement mechanism represents a significant advancement in the field of nanomaterials synthesis with immediate potential for large-scale application in renewable energy technologies.[5,57–61] The renewable energy applications of Pt SGD-synthesized materials are significant because Pt is broadly employed as a catalyst material for both oxygen reduction in hydrogen fuel cells and hydrogen production in photoelectrochemical cells and electrolyzers.[75] Pt materials can also act as useful catalysts for numerous other reactions, including hydrogenation, dehydrogenation, and isomerization.[76] Previous work has shown nanoparticles with varying morphologies and structures possess significantly different electrochemical properties and can be synthesized by only slightly changing reactant conditions.[5,57–61,64,75–81]

To date, a broad parameter space including reactant temperature, solvent, reactant delivery method, reduction potential, and stoichiometry have all been shown to impact the structure and performance of resultant materials.[54,74,82] Reduction potential is dependent on temperature, concentration, and the standard reduction potentials of the template and ions in solution, and thus, alterations thereof can change the rate of displacement.[55,59,67,83] For example, it has been demonstrated that the SGD reaction between Pd nanotubes and chloroplatinic acid is slowed as

concentration of the acid depletes, resulting in a thinner layer of deposited Pt.[67] Stoichiometry also affects morphology: for example, when Au^{+} and Au^{3+} both undergo SGD with Ag nanocubes, Au^{+} deposited three times as much Au since Ag reduces Au^{+} at a 1:1 ratio, while Au^{3+} is reduced at a 1:3 ratio.[84,85] Structure of displaced materials is additionally influenced by size of the template and the use of surface ligands: stronger surface ligands on the Ag particle result in irregular Au nanoparticles with different morphologies than the template,[86] and reducing the size of the Ag spherical template caused hollow Au octahedra to form instead of hollow spheres.[87] Figure 5.2 schematically shows examples of structures synthesized via SGD reactions that were allowed to go to complete conversion.[85−87] Partial conversion of the host material (not shown) offers additional options, such as core−shell structures and alloys that could be advantageous for specific applications.[62−69]

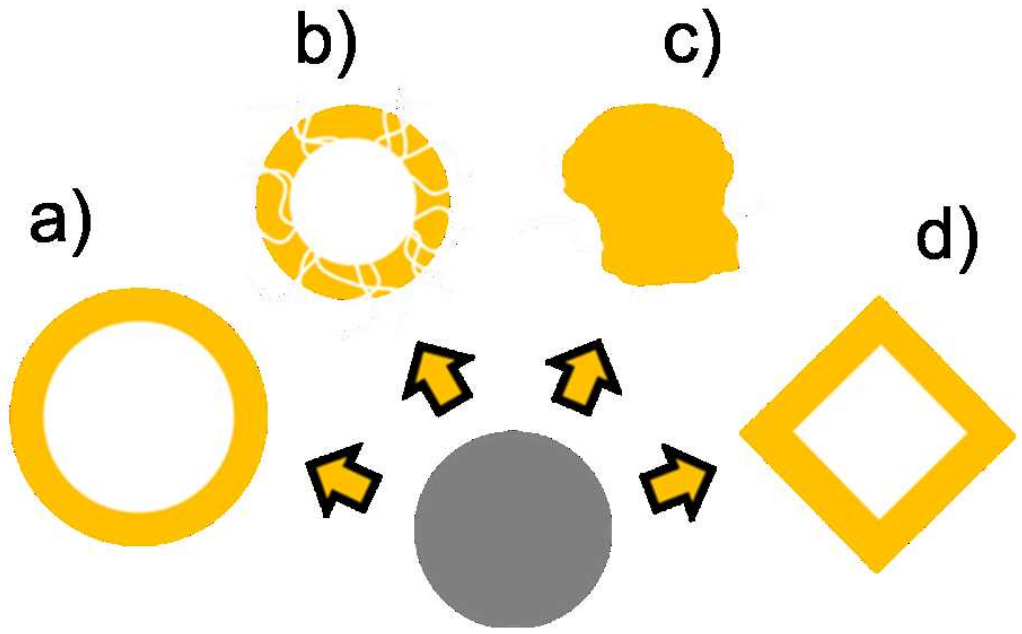

Figure 5.2 (a) SGD of Ag nanoparticles by Au typically produces hollow Au particles of identical morphology. (b) 1:3 Au(III)/Ag stoichiometry can result in porous shell structures, as opposed to solid shells for 1:1 Au(I)/Ag stoichiometry (ref 85). (c) Stronger surface ligands result in irregular Au nanoparticles with different morphologies than the Ag template (ref 86). (d) Small spherical Ag nanoparticle templates produce hollow Au octahedra, as opposed to hollow Au spheres (ref 87).

Experimental[162,65,69–74,77,88–91] and theoretical[79] studies have been conducted to elucidate the mechanism of SGD, often by displacing Ag templates with Au as a model system. The displacement of Ag nanowires by $HAuCl_4$ was studied using *in situ* transmission X-ray microscopy (TXM), revealing that oxidation of Ag initially occurs at sites with high surface energy facets.[89] As Au deposits on the surface, continued oxidation of Ag results in the formation of pits through which Ag from the bulk of the nanowire is oxidized, resulting in formation of a porous nanotube. Pitting and subsequent hollowing of the template greatly influence the morphologies of synthesized structures, for example, when octahedral Au nanocages were obtained via SGD of Ag nanocubes by $HAuCl_4$.[90] Characterization by electron tomography indicated formation of a pit on the [111] facet, through which Ag^+ oxidized from the interior walls of the cube diffused out as Au deposited on the surface. Overlap of Ag and Au signals from 3D electron dispersive X-ray spectroscopy (EDX) mapping suggested formation of an alloy of Au−Ag between layers of Au and Ag. Further addition of $HAuCl_4$ caused dealloying of Ag, resulting in the formation of vacancies in the Au that aggregate via Ostwald ripening to form a single hole on each [111] facet to yield an octahedral nanocage. However, continued dealloying can result in undesirable fragmentation of the synthesized structures due to uncontrolled formation of vacancies. It has been shown that coating a Ag template with a thin layer of Au prior to undergoing SGD yields a more robust structure which preserves the morphology of the template.[91] While oxidation of Ag typically occurs anisotropically at sites with high surface energy, the presence of the Au coating lowers the energy of those sites which slows formation of pores. As Au deposits and pure Ag is oxidized from the template, alloying of Au and Ag occurs both in the walls of the pores and at the interface between the template and coating. Once pure Ag is fully oxidized, dealloying of Au−Ag results in uniform pores on the [111] facets.

While preparation of Au structures from Ag templates is well-studied, further insight into the displacement of Ag by Pt is valuable for tailoring preparations of Pt nanostructures. In this work, SGD reactions between Ag nanowires and K_2PtCl_4 were systematically studied to ascertain the fundamental mechanisms of this versatile materials synthesis method. *Ex situ* microscopy and spectroscopy, combined with X-ray scattering and atom probe tomography (APT), were utilized to gain unique perspective of the SGD processes. With this understanding, PtAg nanotubes were used as advanced nanoscale electrocatalyst materials in fuel cell applications, but Ag dissolution, crossover, and redeposition on the anode in fuel cell tests resulted in poor performance.[92] The lessons learned were subsequently applied to nickel- and cobalt-based Pt nanowires which increased performance without anode deposition challenges.[5,17,93] The advancements achieved in these systems would not have been possible without the knowledge of the SGD process presented in this paper.

5.3 Experimental

Nanowires served as primary model systems as displacement templates due to their spatial symmetry and the ease with which they can be obtained or synthesized. Commercially available Ag nanowires of 60−80 nm diameter and 30 μm length (Nanocs, SNW-01-2) were used as displacement templates for SGD reactions by Pt. The displacement procedure was modified from one previously reported to occur over 2 h.[58] Briefly, Ag nanowires were dispersed in deionized (DI) H2O to 1 mg/mL and 300 mL of solution was heated to 90 °C in an oil bath. A solution of Pt precursor was prepared at 50% molar excess of Pt to Ag by dissolving 0.865 g of K_2PtCl_4 (Sigma-Aldrich, 99.99% trace metals basis) in 10 mL of DI H_2O. The K_2PtCl_4 solution was added via syringe pump (New Era, NE300) over 15 min and allowed to react an additional 0, 2, 5, 10, 15, 60, or 120 min. Aliquots were removed after cooling the reaction to room temperature for *ex situ* measurements. The solutions were then washed three times with saturated NaCl, then three times

by DI H_2O, and additional aliquots of the washed samples were taken. Additional washing was performed by refluxing the 5, 10, 15, 60, and 120 min samples in 4 M HNO_3 for 16 h to remove residual Ag. The reflux was followed by three washes with DI H_2O then three washes of isopropyl alcohol, and aliquots of the refluxed solution were then taken for analysis.

5.3.1 Characterization

Materials were characterized with scanning electron microscopy (SEM), energy dispersive X-ray spectroscopy (EDS), X-ray diffraction (XRD), small-angle Xray scattering (SAXS), and atom probe tomography (APT). SEM and EDS mapping were conducted on a JEOL JSM7000F field emission scanning electron microscope (FESEM) equipped with an EDAX SiLi 30 mm^2 EDS detector. Both XRD and SAXS studies were performed at the Stanford Synchrotron Radiation Lightsource (SSRL): XRD was performed at beamline 11-3 using radiation of λ = 0.976 Å. Scattered X-rays were collected on a MAR345 image plate, with a pixel size of 150 μm and at a sample to detector distance of 200 mm. SAXS studies were performed on beamline 1-4 using radiation of λ = 1.487 Å. Scattered X-rays were collected on a Rayonix SX 165 charge-coupled device (CCD) detector with a pixel size of 79 μm. Data analysis and reduction of SAXS data was performed using the Irena and Nika packages for small-angle scattering (SAS) data analysis plug-in[94] for Igor Pro modeling software. Data was background-subtracted using the scattering from the empty sample holder as the background. Unified fits were applied to the background-subtracted data in order to subtract the Porod and Guinier fit parameters. APT studies were performed on a Cameca LEAP 4000X Si straight flight path instrument using a laser pulse energy of 75 pJ, a pulse frequency of 500 kHz, and a detection rate of 1 ion per 250 pulses at a base temperature of 45.5 K. APT samples were prepared using a method previously developed for analyzing individual nanowires.[95] In short, the particles were dispersed on a 2000 mesh transmission electron microscopy (TEM) grid. Particles were selected and manipulated in a FEI Helios 600i dual-beam

focused ion beam/SEM with an Omniprobe 200 nanomanipulator. Individual particles were moved from the grid onto a post of a sharpened half-TEM grid held by a manipulable holder[96] and attached to the post via electron beam-assisted chemical vapor deposition (CVD). Time-of-flight mass spectrometry within the APT instrument revealed the identity of the field-evaporated species while the two-dimensional detector provided the location of the species. Field evaporation of surface species through the depth of the particle allows for a three-dimensional reconstruction of the composition to be generated.

5.4 Results and Discussion

Ex situ SEM and EDS were used to probe the morphology and elemental composition of Pt nanotubes synthesized from Ag nanowires as shown in Figure 5.3, complementing the X-ray experiments. The images indicate that the macromorphology of the nanotubes was preserved during the SGD process, and EDS shows the majority of displacement of Ag by Pt occurs between 2 and 10 min, as indicated by the increase in Pt wt % from time = 0 to 10 min. Though significant fractions of residual Ag remain well-dispersed throughout the samples as shown by EDS mapping, washing with NaCl and refluxing in HNO_3 removed the majority of this Ag, yielding a nanotube primarily composed of Pt as shown in Figure 5.4 by the high Pt wt % in washed samples. Washing was performed to remove AgCl and Ag from the PtAg nanowires as these materials were prepared for use as fuel cell electrocatalysts, in which standard operating conditions would cause Ag to oxidize. Ag^+ would then diffuse to the anode and be reduced, forming Ag deposits that negatively impact performance.[58]

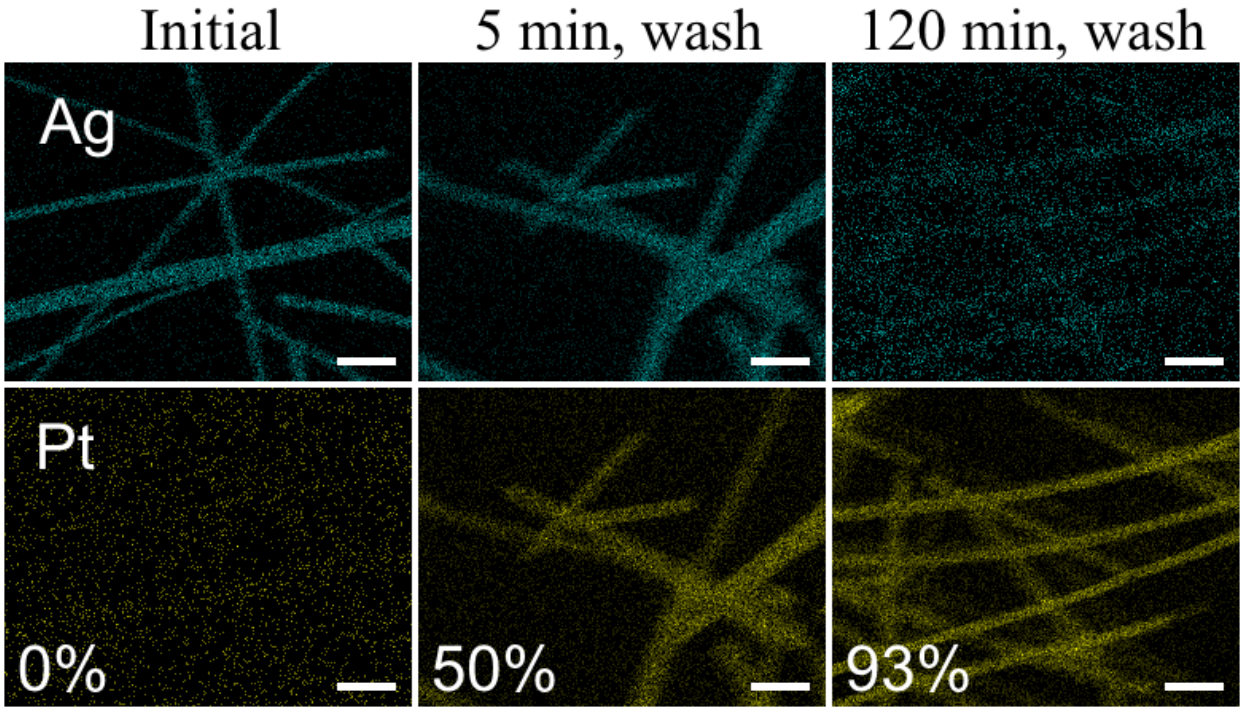

Figure 5.3 Elemental mapping from SEM of PtAg nanotubes made via SGD of Ag nanowires after reaction times of 0, 5, and 120 min, with Pt wt % listed. The 5 and 120 min samples were washed with NaCl solution, then refluxed in HNO_3 to remove residual Ag on the surfaces of the nanotubes. Scale bars are 500 nm.

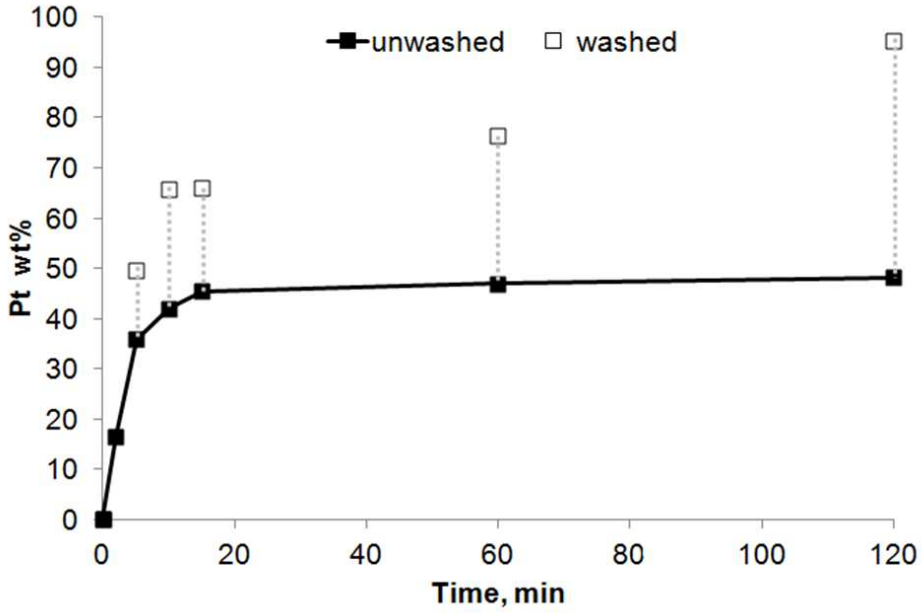

Figure 5.4 Pt wt % as a function of reaction time and cleaning with NaCl, then HNO_3.

5.4.1 X-ray Characterization

In order to probe the morphological changes taking place during the SGD process, a combination of *ex situ* techniques were used to study the structure and morphology of the single-walled PtAg nanotubes. These included the complementary experimental techniques of XRD to probe crystal structure and SAXS to probe particle size.

Ex situ studies of the process were performed to acquire "snapshots" at various extents of reaction. Correlating the results of the complementary experimental measurements allowed for the development of an improved fundamental understanding of the process leading to tailored synthesis of nanomaterials with specific shape and composition. The measurements provided information regarding the extent of alloying that occurs as a function of displacement and observation of morphological changes from the atomic to the nanoscale over the course of the SGD process. XRD plots of NaCl washed PtAg nanotubes synthesized from Ag nanowire templates at several points in the reaction are shown in Figure 5.5, and parameters of the data are shown in Table 1. The Ag(111) peak is shown as a dashed black line at q = 2.661 $Å^{-1}$, and the Pt(111) peak at q = 2.773 $Å^{-1}$ is shown as a solid black line for reference. XRD plots indicate the q vector, and hence lattice parameter, of the Ag nanowires at q = 2.667 $Å^{-1}$ is similar to that of bulk Ag, but after 2 min the peak shifts to q = 2.688 $Å^{-1}$ as a second peak at q = 2.742 $Å^{-1}$ develops. The presence of both peaks indicates the development of alloyed regions on the nanotube: one phase enriched in Ag at low q, and one enriched in Pt at high q. It has been shown that alloyed PtAg nanomaterials closely conform to Vegard's law:[97,98]

$$d = d_2\left(1 + \frac{d_1 - d_2}{d_2}\chi_1\right)$$

where d, d_1, and d_2 are the lattice parameters of a bimetallic alloy and the pure metals that compose it and χ_1 is the molar fraction of pure metal 1 present.[99] Thus, composition of the alloy can be

computed from the position of its peak maxima by using $q = \frac{2\pi}{d}$: the two peaks in the 2 min sample have compositions of 75 atom % Ag and 25 atom % Ag, respectively, as shown in Table 1. At 5 min, further displacement by Pt causes the two distinct signals to overlap, forming a single peak at q = 2.692 $Å^{-1}$ and 70 atom % Ag with a broad shoulder seen at higher q. This indicates a single PtAg alloy composition becomes dominant in the PtAg nanotube, with other compositions present in decreased amounts. As displacement continues the nanotubes anneal to reach a final PtAg ratio of 40 atom % Ag and 60 atom % Pt, indicated by a shift to q = 2.726 $Å^{-1}$ after 120 min. The decrease in Ag atom % may also be indicative of a dealloying process in the nanowire: after all Ag in the template has been oxidized, further reduction of Pt^{2+} only occurs as Ag in the Pt−Ag alloy is oxidized, creating vacancies that anneal to form pores in the surface. Although bulk PtAg alloys are unfavorable due to a difference in lattice spacing of 4.3%, PtAg alloyed nanostructures have been previously reported.[58,65,71] Although XRD indicates the 60 min sample had higher Pt atom % than the 120 min sample, it should be noted that the difference in peak position of the samples differs by q = 0.008 $Å^{-1}$. Since each pixel on the detector can measure a change of q = 0.009 $Å^{-1}$ with the instrumental parameters used, the change is within the error of the instrument. The narrowing of full peak width at half-maximum (fwhm) from 0.084 to 0.064 $Å^{-1}$ indicates growth of crystallites during annealing: assuming the crystallites are spherical and no change in degree of disorder occurs, their coherence length is given by $d = \frac{2\pi}{fwhm}$ and thus corresponds to growth from 75 to 97 Å. The XRD plots indicate three major steps in the SGD process: initial formation of PtAg alloys over the first 2 min, development of one primary composition after 5 min, and annealing to reach final composition over the rest of the 120 min reaction as shown in Figure 5.6. These steps correspond to the change in Pt wt % over time obtained from EDS, shown in Figure 5.4.

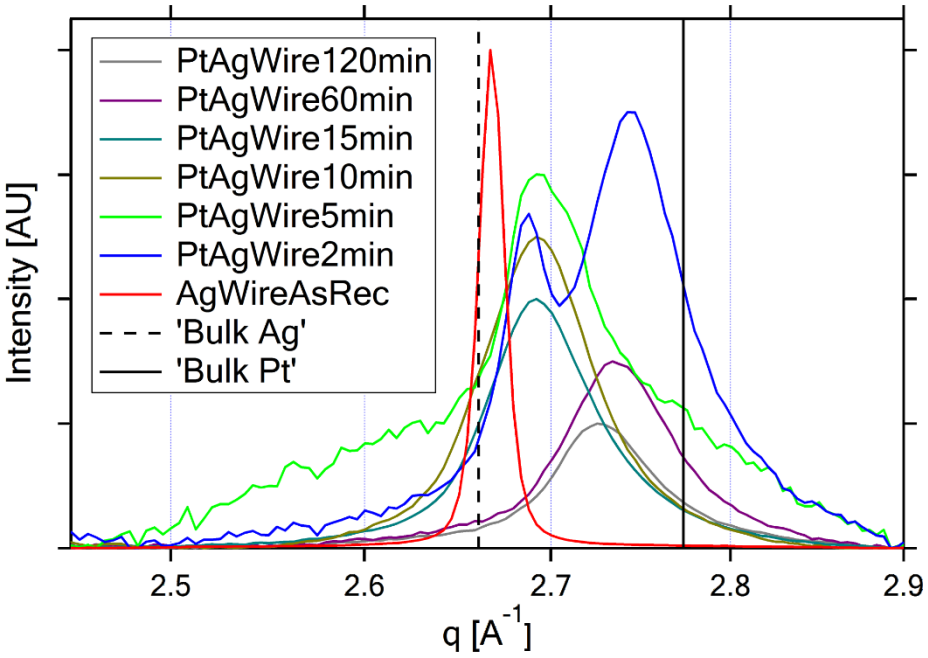

Figure 5.5 Ex situ XRD plots of arbitrary intensity show the shift in peak from Ag to Pt during the displacement process; an overall shift from q = 2.667 to 2.726 $Å^{-1}$ is observed.

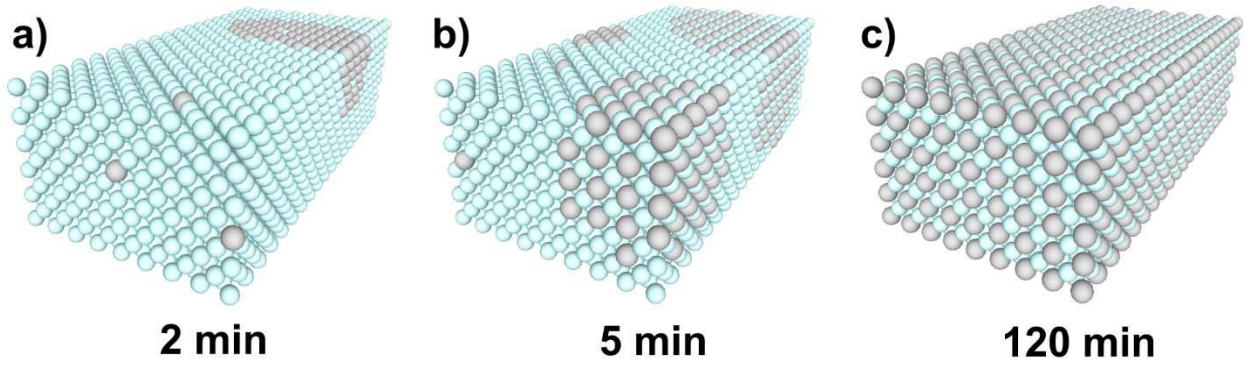

Figure 5.6 Schematic of SGD reaction, with Ag atoms (blue) and Pt atoms (gray). (a) After initial displacement both silver-rich and platinum-rich regions are present in the nanotube. (b) After 5 min, continued deposition results in formation of a primary PtAg alloy, though regions enriched in either Pt or Ag are still present. (c) Final composition is reached after 120 min.

SAXS data were collected in addition to XRD on the same aliquots of solution for both as-synthesized and NaCl washed nanotubes. The unwashed samples more clearly show changes in curve shape (Figure 5.7), which indicate that the mesoscale morphology of the PtAg nanotubes is changing during the reaction. Features develop in the SAXS curve after 2 min and change significantly between 2 and 10 min; these times correspond to the rapid increase in Pt wt % seen

in Figure 5.4 during the first 10 min of the reaction. Modeling was performed on the SAXS data by applying the Unified Fit method from the Irena package for Igor Pro, yielding a Guinier curve and Porod's law function for each population of scattered atoms in the sample. Scattering occurs when an interface is present in the sample which is characterized by the unified fitting parameters: the Guinier curve yields the radius of gyration (Rg) which is representative of the size of the scattering object, and the Porod's law constant (P) varies according to the nature of the interface of the particles and their surrounding matrix; a value of P = 4 indicates a clean interface, while P = 3 indicates a rough, porous interface.

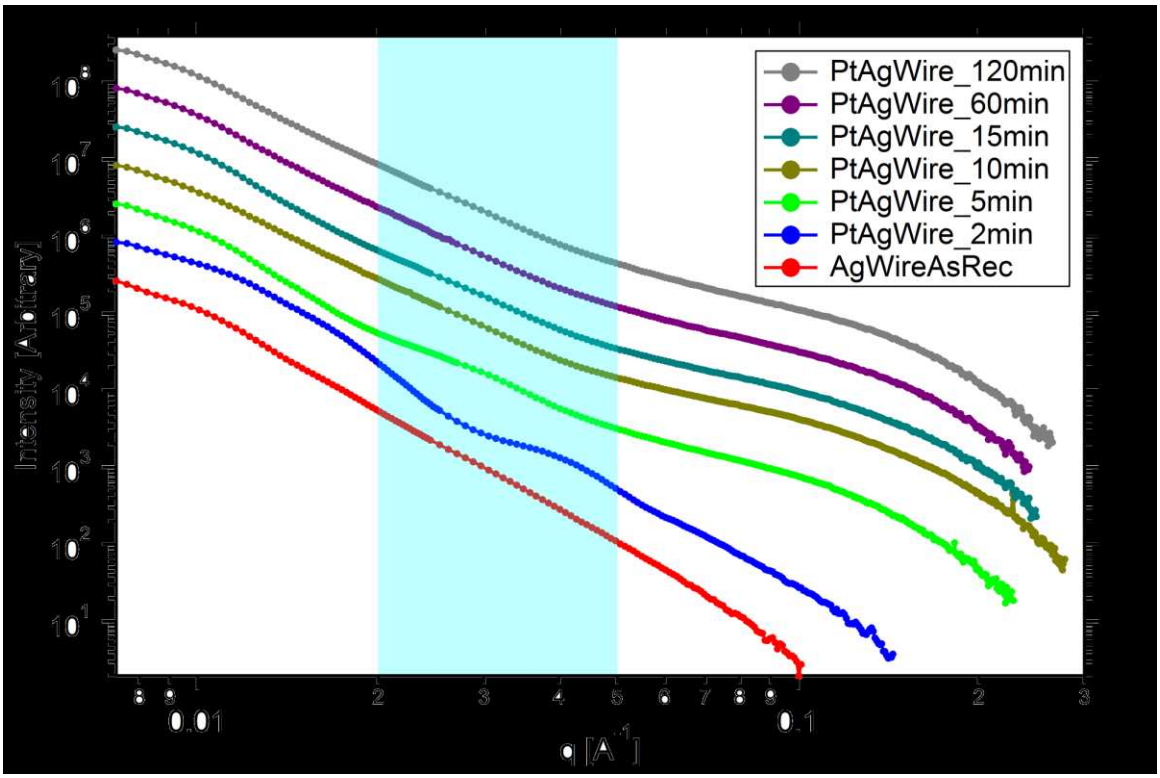

Figure 5.7 SAXS data of PtAg nanotube materials synthesized by SGD. Between 2 and 10 min, changes in intensity occur in the q ≈ 0.02−0.05 $Å^{-1}$ region (highlighted).

Unified fits of both as-synthesized and NaCl washed samples are shown in Figure 5.8 and Figure 5.S1 with each scatterer population labeled, corresponding to fitting parameters provided in Tables 5.S1 and 5.S2. The Ag nanowires have only one scatterer present at Rg = 256 Å (⬠),

which is smaller than the crystallite size obtained in the XRD. After 2 min, three levels of scatterers can be seen at Rg = 205.4, 48.4, and 39.2 Å labeled as ⬠, ↑, and ∧, respectively. As Pt deposition results in PtAg alloys, the second and third populations could be attributed either to the boundary between platinum-enriched and silver-enriched regions, or to pore formation on the nanotube. Pore formation readily occurs in SGD reactions when stoichiometry of the cations in solution and template atoms is not 1:1.[54,84,85,89–91] For the displacement of Ag^0 by Pt^{2+}, the stoichiometry is $2Ag^0 + PtCl_4^{2-} \rightarrow 2AgCl + 2Cl^- + Pt^0$. The smallest population's Rg (∧) decreases to 17.1 Å by 5 min and varies little for the rest of the reaction, while the second population's Rg (↑) increases to 102.0 Å by 10 min and changes to 107.5 Å after 120 min. The changes occurring between the 2 and 10 min sample correspond to development of the primary PtAg alloy, as do the small changes between 10 and 120 min to the annealing of the sample. Since the Rg of the second population is similar to the crystallite size obtained from XRD for each sample, we interpret this feature as arising from the interfaces between PtAg alloyed regions in the Pt matrix. The population with smallest Rg (∧) is attributed to pores on the surface of the nanowire instead of deposited AgCl since the population is present in both as-synthesized and washed samples: after initial formation, continued deposition of Pt reduces their size. Additional evidence for this assignment of the populations is seen in the P constants of each level: the P constant of the smallest population remains constant at 4.0, while the second population decreases from 4.0 to 3.2 in the 5 min sample. The decrease in P indicates roughening of the interface and can be attributed to alloying of Ag by Pt. The washing process of the particles causes features in the SAXS data (Figure 5.9) to become more readily apparent as Ag in the form of AgCl is washed from the PtAg nanotube by saturated NaCl solution via salt solubilization effect, and is seen as changes in the Rg and P of the second population (↑) of the unified fit between as-synthesized and washed samples given in Tables S1 and S2. SAXS, wide-

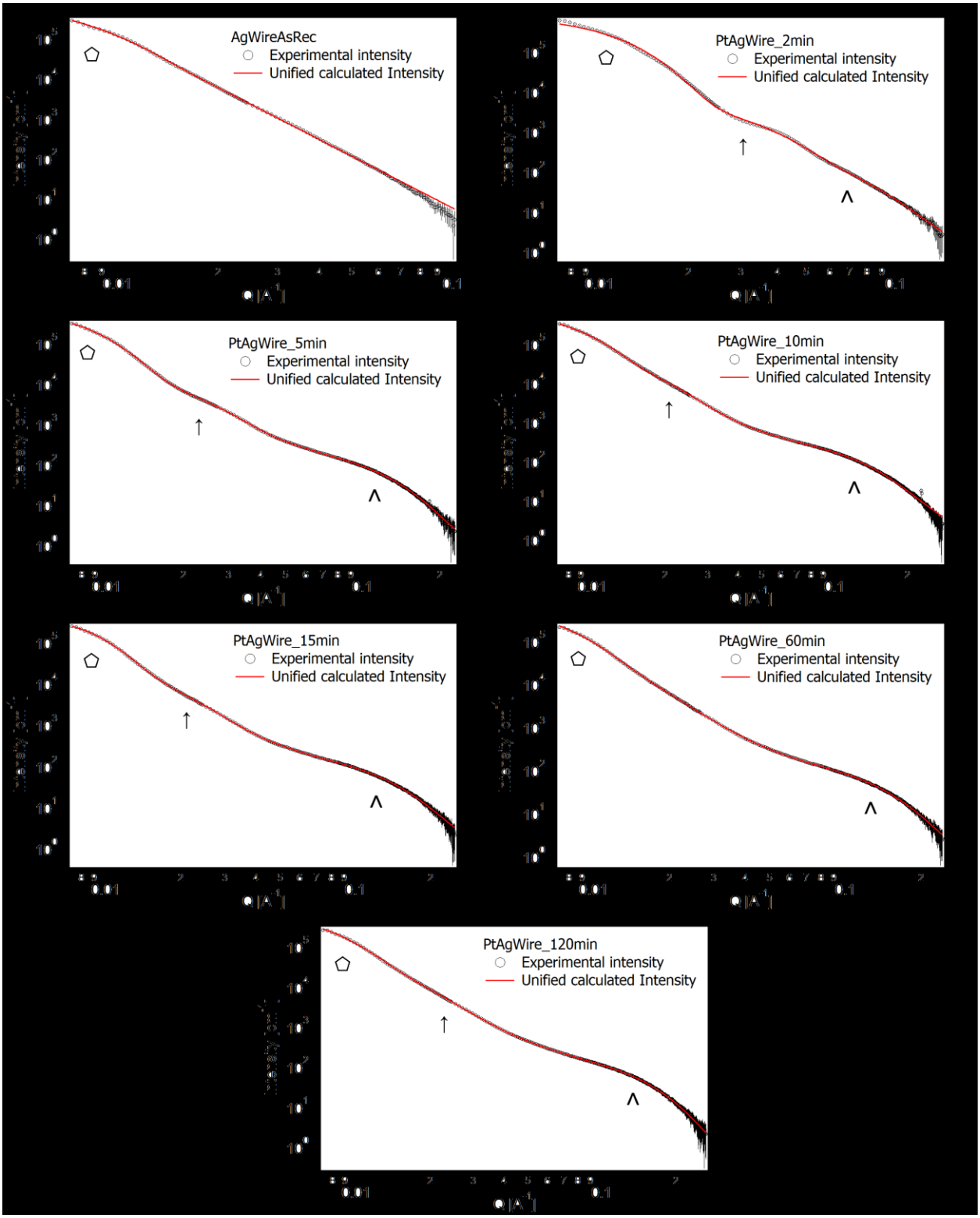

Figure 5.8 Unified fits for samples prior to NaCl washing. Labeled regions correspond to the first (⬠), second (↑), and third (∧) populations of scatterers present.

angle X-ray scattering (WAXS), and EDS all indicate that there are three stages in the SGD process: WAXS shows the development of PtAg alloys and crystallite size, which corresponds to the size scale of the features observed by SAXS. Composition of the nanotube, as well as shape of the crystallites, was then further elucidated by atom probe tomography.

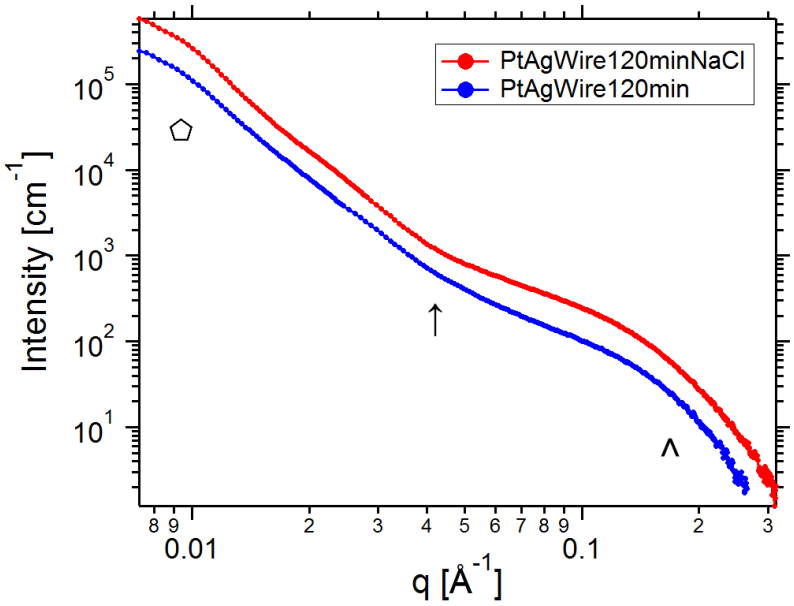

Figure 5.9 SAXS data of PtAg nanotubes before and after cleaning with NaCl solution and HNO_3. Features are more strongly defined in the q ≈ 0.03−0.10 Å^{-1} region labeled by ↑, corresponding to the second population of scatterers in the unified fit.

5.4.2 Atom Probe Tomography

Atom probe tomography (APT) was used to examine the 3D atomic composition of a single NaCl washed PtAg nanotube to examine the heterogeneity of displacement of the Ag by Pt. Figure 5.S2 depicts the sample preparation, where a nanomanipulator mechanically transfers a single nanotube from the grid onto a post for atom probe analysis. The APT data were used to generate three-dimensional reconstructions. The SEM imaging and manipulation indicated that these particles were hollow tube structures with some of the particles having closed ends. The APT results supported this observation in that the initial evaporation filled the detector but continued analysis resulted in a ring-shaped histogram of detected species. The composition of the analyzed

region was found to be 3:1 Pt/Ag atomic ratio or 84 wt % Pt, differing slightly from the 93 wt% Pt found from SEM EDS, though this lies within the error of the instrument used for EDS. The nanotube tip composition differs from that of the overall nanotube, evidenced by the twodimensional projections of the compositions along the long axis of a washed 120 min PtAg nanotube as shown in Figure 5.10 and the three-dimensional reconstruction shown in Video S1. The projections reveal the extent of heterogeneity in the composition of the particles, indicating that the SGD process did not occur to completion. The largest remaining silver-rich clusters contained 70−80 atom % Ag and were irregularly shaped, spanning regions up to 30 nm across. The slight difference in wt % of Pt between SEM EDS and APT is within the error of the instrument used and can also be attributed to the small sampling volume analyzed by APT. XRD plots show the PtAg nanotube peak occurs at q in between the Ag and Pt references, which can be attributed to the presence of residual Ag which was detected by APT. The silver-enriched regions were found to exist in clusters of aspect ratio of 2−3 which have a thickness of approximately 4 nm, which differs from the Rg values found from the SAXS unified fits and occurs since X-ray techniques yield data from all sample along the path of the beam, resulting in a larger analyzed volume than APT.

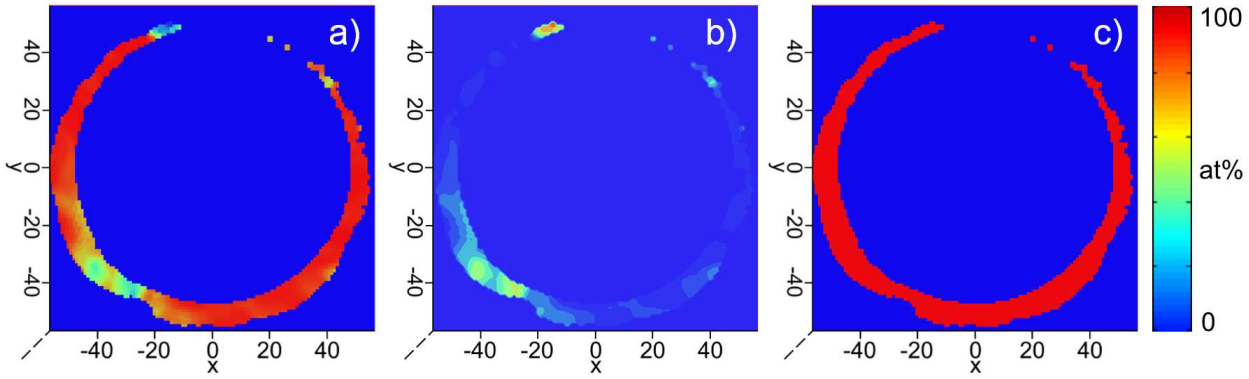

Figure 5.10 Two-dimensional projection of an APT reconstruction from 15 nm below the closed end of a washed 120 min nanotube showing atom % of (a) Pt, (b) Ag, and (c) Pt + Ag. Axis dimensions are in nanometers.

5.5 Conclusion

Materials synthesis by SGD is potentially a game-changing advancement toward materials by design. These materials are of interest because of their close tie to renewable energy applications, where SGD can be applied to anisotropic materials in which long-range connectivity aids in long-range electron transport – a critical property in renewable energy applications such as fuel cells. The compositional control provides a powerful capability to tune the material properties of nanomaterials, leading to designed materials that have not been previously demonstrated and may only be possible through SGD. XRD and SAXS analysis reveal a compositional change and the development of a rough surface on the nanotubes as Ag is displaced by Pt over the course of the SGD reaction, indicating the formation of 10 nm crystallites and 1–2 nm pores, while the macrostructure of the material is maintained. APT yields insight of the degree to which displacement occurs in the material and the resulting 3D nanoscale structure, supporting the XRD plots and revealing the hollow interior of the PtAg nanotubes. The results corroborate that SGD primarily occurs in a short time span at the start of the reaction, oxidizing Ag both from the surface and center of the nanowire as Pt is deposited. The analytical techniques used are suitable for analyzing materials produced via SGD and could be applied to applications in other systems.

5.6 Associated Content

The Supporting Information is available free of charge on the ACS Publications website at DOI: 10.1021/acs.jpcc.6b07363.

- Unified fit parameters of as-synthesized and NaCl washed PtAg nanotubes, unified fits of NaCl washed PtAg nanotubes, and mounting of PtAg nanotube onto post for atom probe tomography (PDF)
- Video showing three-dimensional composition of a PtAg nanotube (AVI)

5.7 Author Information

Corresponding Author: *E-mail: rrichard@mines.edu. Phone: 303-273-3612.

Author Contributions: ⊥ M.B.S. and G.J.L. contributed equally to this work.

Notes: The authors declare no competing financial interest.

5.8 Acknowledgements

This work is funded by the Laboratory Directed Research and Development (LDRD) Program at the National Renewable Energy Laboratory, under contract award UGA-0-41025-63. NREL is a national laboratory of the U.S. Department of Energy, Office of Energy Efficiency and Renewable Energy, operated by the Alliance for Sustainable Energy, LLC. Use of the Stanford Synchrotron Radiation Lightsource, SLAC National Accelerator Laboratory, is supported by the U.S. Department of Energy, Office of Science, Office of Basic Energy Sciences under contract no. DE-AC02-76SF00515. The atom probe used in this work was funded through the NSF by Major Research Instrumentation Grant No. 1040456.

CHAPTER 6

SUMMARY AND FUTURE WORK

6.1 Summary of Work

In order to reduce the cost and improve stability of catalysts used in polymer electrolyte membrane fuel cells (PEMFCs), this thesis addressed the development and characterization of model N-doped high-surface area substrates. A series of N-doped carbon nanospheres (N-CS) were developed by adjusting synthesis parameters, such as EDA concentration and pyrolization temperature, resulting in materials suitable for characterization by novel techniques such as atom probe tomography (APT). The N-CS synthesis was modified by addition of a variety of Fe precursors to obtain a series of Fe-N-C with varied compositions targeting formation of atomically dispersed Fe. Fe precursor and pyrolization temperature were found to impact loading of Fe as well as frequency of Fe nanoparticles. N-CS were also utilized as a substrate to develop PGM catalysts with well-dispersed Pt nanoparticles of 2-4 nm in size (Pt/NC) for further studies of interactions between N-functionalities in the support and Pt nanoparticles. Pt-based materials produced via SGD were also characterized to improve fundamental understanding of the SGD mechanism, enabling better control of synthesis of new catalysts.

6.2 Future Work

The materials developed in this work are appropriate for further characterization by electrochemical testing on rotating disc electrode (RDE) to evaluate the activity of prepared PGM and PGM-free catalysts. Novel characterization techniques can then be used to correlate activity with changes in atomic composition determined via APT, nanoparticle dispersion via in-situ microscopy, and surface composition under non-vacuum conditions via ambient pressure XPS (AP-XPS).

6.2.1 Atom Probe Tomography of Materials

APT can yield 3D atomic reconstructions of a sample, thereby complementing data obtained from XPS and EDS. XPS is surface sensitive, but probes the top 10 nm and averages signal over a large (700 x 300 μm). EDS has nanometer resolution but is 2D; information gained from APT would be both on an atomic scale and 3D, thus complementing both XPS and EDS. Performing APT on N-CS and Fe-N-C would provide better understanding of how N and Fe are distributed in the material, highlighting differences between true surface, sub-surface, and the bulk. These results could potentially correlate to differences in electrochemical activity, and would mark the first time carbon-based materials have been examined by APT.

To facilitate APT analysis of a large number of samples, further improvements to the sample preparation procedure remain to be made. In particular, loss of the tip within the APT instrument could be prevented by utilizing an immobile medium with evaporation field similar to that of C, instead of the Au currently used. Identification of a suitable element and development of a procedure to immobilize materials of interest within it would prevent accidental sample loss during analysis, a major concern which presently hinders the analysis of large series of samples via APT.

6.2.2 *In Situ* Characterization

In-situ microscopy combined with electrochemistry allows for imaging of catalyst material during electrochemical cycling. For PGM catalysts such as the Pt/NC prepared in Chapter 4, this allows correlations to be made between nanoparticle size and dispersion and the catalytic activity with time. By comparing Pt/NC prepared on substrates with varied compositions, changes in dispersion and activity can then be related to N concentration and functionalities on the surface of the N-CS substrate.

AP-XPS allows surface composition of materials to be measured during conditions that are similar to those of an operating fuel cell, including elevated temperature and presence of atmosphere containing O_2 and H_2O. This technique can provide information about adsorption sites and interactions of O_2 with the catalyst surface.

REFERENCES

[1] Y. Huang, J. Zhang, A. Kongkanand, F. T. Wagner, J. M. C. Li, J. Jorné, *J. Electrochem. Soc.* **2014**, 161, F10-F15

[2] K. Sasaki, H. Naohara, Y. Cai, Y. M. Choi, P. Liu, M. B. Vukmirovic, J. X. Wang, R. R. Adzic. *Angew. Chem. Int. Ed.* **2010**, *49*, 8602-8607

[3] A. Schenk, C. Grimmer, M. Perchthaler, S. Weinberger, B. Pichler, C. Heinzl, C. Scheu, F.-A. Mautner, B. Bitschnau, V. Hacker, *J. Pow. Sources* **2014**, 266, 313-322

[4] D. Wang, H. L. Xin, R. Hovden, H. Wang, Y. Yu, D. A. Muller, F. J. DiSalvo, H. D. Abruña. *Nat. Mater.* **2013**, *12*, 81-87

[5] S. M. Alia, S. Pylypenko, K. C. Neyerlin, D. A. Cullen, S. S. Kocha, B. S. Pivovar. *ACS Catal.* **2014**, *4*, 2680-2686

[6] Y. Shao-Horn, W. C. Sheng, S. Chen, P. J. Ferreira, E. F. Holby, D. Morgan. *Top. Catal.* **2007**, *46*, 285-305

[7] R. Borup, J. Meyers, B. Pivovar, Y. S. Kim, R. Mukundan, N. Garland, D. Myers, M. Wilson, F. Garzon, D. Wood, P. Zelenay, K. More, K. Stroh, T. Zawodzinski, J. Boncella, J. E. McGrath, M. Inaba, K. Miyatake, M. Hori, K. Ota, Z. Ogumi, S. Miyata, A. Nishikata, Z. Siroma, Y. Uchimoto, K. Yasuda, K. Kimijima, N. Iwashita. *Chem. Rev.* **2007**, *107*, 3904-3951

[8] J. Xie, D. L. Wood III, K. L. More, P. Atanassov, Rodney L. Borup. *J. Electrochem. Soc.* **2005**, *152*, A1011-A1020

[9] R. K. Ahluwalia, S. Arisetty, J.-K. Peng, R. Subbaraman, X. Wang, N. Kariuki, D. J. Myers, R. Mukundan, R. Borup, O. Polevayac. *J. Electrochem. Soc.* **2014**, *161*, F291-F304

[10] E. Ruckenstein, B. Pulvermacher. *J. Catal.* **1973**, *29*, 224-245

[11] F. Ettingshausen, J. Kleemann, A. Marcu, G. Toth, H. Fuess, C. Roth. *Fuel Cells* **2011**, *11*, 238-245

[12] L. M. Roen, C. H. Paik, T. D. Jarvi. *Electrochem. Solid-State Lett.* **2004**, *7*, A19-A22

[13] K. Kinoshita. *Carbon: Electrochemical and Physicochemical Properties*; Wiley: New York, 1988

[14] V. Jalan, E. J. Taylor. *J. Electrochem. Soc.* **1983**, 130, 2299-2302

[15] D. van der Vliet, C. Wang, M. Debe, R. Atanasoski, N. M. Markovic, V. R. Stamenkovic. *Electrochim. Acta* **2011**, *56*, 8695-8699

[16] K. A. Kuttiyiel, K. Sasaki, Y.M. Choi, D. Su, P. Liu, R. R. Adzic. *Nano Lett.* **2012**, *12*, 6266-6271

[17] S. M. Alia, B. A. Larsen, S. Pylypenko, D. A. Cullen, D. R. Diercks, K.C. Neyerlin, S. S. Kocha, B. S. Pivovar. *ACS Catal.* **2014**, *4*, 1114–1119

[18] M. Li, Y. Lei, N. Sheng, T. Ohtsuka. *J. Power Sources* **2015**, *294*, 420-429

[19] J. Hu, K. A. Kuttiyiel, K. Sasaki, D. Su, T.-H. Yang, G.-G. Park, C. Zhang, G. Chen, R. R. Adzic. *Catalysts* **2015**, *5*, 1321-1332

[20] J. Marcinkoski, J. Spendelow, A. Wilson, D. Papageorgopoulos. U.S. Department of Energy 2015, <https://www.hydrogen.energy.gov/pdfs/15015_fuel_cell_system_cost_2015.pdf>

[21] F. Jaouen, J. Herranz, M. Lefèvre, J.-P. Dodelet, U. I. Kramm, I. Herrmann, P. Bogdanoff, J. Maruyama, T. Nagaoka, A. Garsuch, J. R. Dahn, T. Olson, S. Pylypenko, P. Atanassov, E. A. Ustinov. *ACS Appl. Mater. Interfaces* **2009**, *1*, 1623-1639

[22] G. Wu, P. Zelenay. *Acc. Chem. Res.* **2013**, *46*, 1878-1889

[23] M. Lefèvre, E. Proietti, F. Jaouen, J.-P. Dodelet, *Science* **2009**, *324*, 71-74

[24] R. Kothandaraman, V. Nallathambi, K. Artyushkova, S. C. Barton. *Appl. Catal. B* **2009**, *92*, 209-216

[25] H. T. Chung, C. M. Johnston, K. Artyushkova, M. Ferrandon, D. J. Myers, P. Zelenay. *Electrochem. Comm.* **2010**, *12*, 1792-1795

[26] M. Ferrandon, A. J. Kropf, D. J. Myers, K. Artyushkova, U. Kramm, P. Bogdanoff, G. Wu, C. M. Johnston, P. Zelenay. *J. Phys. Chem. C* **2012**, *116*, 16001-16013

[27] N. Leonard, V. Nallathambi, S. C. Barton. *J. Electrochem. Soc.* **2013**, *160*, F788-F792

[28] J. Li, S. Ghoshal, W. Liang, M.-T. Sougrati, F. Jaouen, B. Halevi, S. McKinney, G. McCool, C. Ma, X. Yuan, Z.-F. Ma, S. Mukerjee, Q. Jia. *Energy Environ. Sci.* **2016**, *9*, 2418-2432

[29] G. Wu, K. L. More, C. M. Johnston, P. Zelenay, *Science* **2011**, *332*, 443-447

[30] J. Y. Cheon, T. Kim, Y.M. Choi, H. Y. Jeong, M. G. Kim, Y. J. Sa, J. Kim, Z. Lee, T.-H. Yang, K. Kwon, O. Terasaki, G.-G. Park, R. R. Adzic, S. H. Joo1. *Sci. Rep.* **2013**, *3*, 2715-1 to 8

[31] K. Lee, L. Zhang, H. Lui, R. Hui, Z. Shi, J. Zhang. *Electrochim. Acta* **2009**, *54*, 4704-4711

[32] Z.-S. Wu, L. Chen, J. Liu, K. Parvez, H. Liang, J. Shu, H. Sachdev, R. Graf, X. Feng, K. Müllen. *Adv. Mater.* **2014**, *26*, 1450-1455

[33] X. Li, H. Wang, H. Yu, Z. Liu, F. Peng, *J. Pow. Sources* **2014**, 260, 1-5

[34] Y. Jiao, Y. Zheng, M. Jaroniec, S. Z. Qiao, *J. Am. Chem. Soc.* **2014**, 136, 4394-4403

[35] N. Matsuda, T. Nakashima, T. Kato, H. Shiroishi, *Electrochim. Acta* **2014**, 146, 73-78

[36] W. Song, Z. Chen, C. Yang, Z. Yang, J. Tai, Y. Nan, H. Lu, *J. Mater. Chem. A* **2015**, 3, 1049-1057

[37] A. Serov, K. Artyushkova, E. Niangar, C. Wang, N. Dale, F. Jaouen, M.-T. Sougrati, Q. Jia, S. Mukerjee, P. Atanassov. *Nano Energy* **2015**, *16*, 293-300

[38] K. N. Wood, R. O'Hayre, S. Pylypenko. *Environ. Sci.* **2014**, *7*, 1212-1249

[39] Y. Chen, J. Wang, H. Liu, R. Li, X. Sun, S. Ye, S. Knights, *Electrochem. Commun.* **2009**, *11*, 2071–2076

[40] X. Sun, Y. Zhang, P. Song, J. Pan, L. Zhuang, W. Xu, W. Xing. *ACS Catal.* **2013**, *3*, 1726-1729

[41] D. Higgins, M. A. Hoque, M. H. Seo, R. Wang, F. Hassan, J.-Y. Choi, M. Pritzker, A. Yu , J. Zhang, Z. Chen, *Adv. Funct. Mater.* **2014**, 24, 4325-4336

[42] S. Shanmugam, J. Sanetuntikul, T. Momma, T. Osaka, *Electrochim. Acta* **2014**, 137, 41-48

[43] N. Cheng, J. Liu, M. N. Banis, D. Geng, R. Li, S. Ye, S. Knights, X. Sun, *Int. J. Hydr. En.* **2014**, 39, 15967-15974

[44] Z. Liu, J. Qu, X. Fu, Q. Wang, G. Zhong, F. Peng, *Mater. Lett.* **2015**, 142, 115-118

[45] S. Gouse Peera, A.K. Sahu, A. Arunchander, S.D. Bhat, J. Karthikeyan, P. Murugan. *Carbon* **2015**, *93*, 130-142

[46] N. P. Wickramaratne, J. Xu, M. Wang, L. Zhu, L. Dai, M. Jaroniec. *Chem. Mater.* **2014**, *26*, 2820-2828

[47] J. Liu, S. Z. Qiao, H. Liu, J. Chen, A. Orpe, D. Zhao, G. Q. (M.) Lu. *Angew. Chem. Int. Ed.* **2011**, *50*, 5947-5951

[48] S. Pylypenko, A. Queen, T. S. Olson, A. Dameron, K. O'Neill, K. C. Neyerlin, B. Pivovar, H. N. Dinh, D. S. Ginley, T. Gennett, R. O'Hayre. *J. Phys. Chem. C* **2011**, *115*, 13667-13675

[49] I. Kusunoki, M. Sakai, Y. Igari, S. Ishidzuka, T. Takami, T. Takaoka, M. Nishitani-Gamo, T. Ando. *Surf. Sci.* **2001**, *492*, 315-328

[50] S. Pylypenko, S. Mukherjee, T. Olson, P. Atanassov. *Electrochim. Acta* **2008**, *53*, 7875-7883

[51] D. Guo, R. Shibuya, C. Akiba, S. Saji, T. Kondo, J. Nakamura. *Science* **2016**, *351*, 361-365

[52] X. Ning, Y. Li, H. Yu, F. Peng, H. Wang, Y. Yang. *J. Catal.* **2016**, *335*, 95-104

[53] X. Ning, Y. Li, B. Dong, H. Wang, H. Yu, F. Peng, Y. Yang. *J. Catal.* **2017**, *348*, 100-109

[54] P. R. Sajanlal, T. S. Sreeprasad, A. K. Samal, T. Pradeep. *Nano Reviews* **2011**, *2*, 5883-1 - 5883-62

[55] S. R. Brankovic, J. X. Wang, R. R. Adzic. *Surf. Sci*. **2001**, *474*, L173-L179

[56] J. Turkevich, G. Kim. *Science* **1970**, *169*, 873-879

[57] S. Guo, S. Dong, E. Wang. *J. Phys. Chem. C* **2009**, 113, 5485-5492

[58] B. A. Larsen, K. C. Neyerlin, J. B. Bult, C. Bochert, J. L. Blackburn, S. S. Kocha, B. S. Pivovar. *J. Am. Chem. Soc.* **2012**, *159*, F622-F627

[59] J. W. Hong, S. W. Kang, B.-S. Choi, D. Kim, S. B. Lee, S. W. Han. *ACS Nano* **2012**, 6, 2410-2419

[60] M. Wang, W. Zhang, J. Wang, A. Minett, V. Lo, H. Liu, J. Chen. *J. Mater. Chem. A* **2013**, *1*, 2391-2394

[61] Z. Chen, M. Waje, W. Li, Y. Yan. *Angew. Chem. Int. Ed*. **2007**, *46*, 4060-4063

[62] Y. Sun, Y. Xia. *J. Am. Chem. Soc.* **2004**, *126*, 3892-3901

[63] Y. Chen, F. Yang, Y. Dai, W. Wang, S. Chen. *J. Phys. Chem. C* **2008**, *112*, 1645-1649

[64] J. R. Croy, S. Mostafa, L. Hickman, H. Heinrich, B. R. Cuenya. *Appl. Catal. A* **2008**, *350*, 207-216

[65] W. Zhang, J. Yang, X. Lu. *ACS Nano* **2012**, *6*, 7397-7405

[66] C. Koenigsmann, A. C. Santulli, K. Gong, M. B. Vukmirovic, W.-P. Zhou, E. Sutter, S. S. Wong, R. R. Adzic. *J. Am. Chem. Soc.* **2011**, *133*, 9783-9795

[67] H. Zhang, M. Jin, H. Liu, J. Wang, M. J. Kim, D. Yang, Z. Xie, J. Liu, Y. Xia. *ACS Nano* **2011**, *5*, 8212-8222

[68] S. M. Alia, K. O. Jensen, B. S. Pivovar, Y. Yan. *ACS Catal.* **2012**, *2*, 858-863

[69] Y. Xing, Y. Cai, M. B. Vukmirovic, W.-P. Zhou, H. Karan, J. X. Wang, R. R. Adzic. *J. Phys. Chem. Lett.* **2010**, *1*, 3238-3242

[70] J. Zhang, F. H. B. Lima, M. H. Shao, K. Sasaki, J. X. Wang, J. Hanson, R. R. Adzic. *J. Phys. Chem. B* **2005**, *109*, 22701-22704

[71] C.-L. Lee, C.-M. Tseng. *J. Phys. Chem. C* **2008**, *112*, 13342-13345

[72] C.-L. Lee, C.-M. Tseng, R.-B. Wu. *Electrochem. Comm.* **2009**, *11*, 627-630

[73] C. J. Dotzler, B. Ingham, B. N. Illy, K. Wallwork, M. P. Ryan, M. F. Toney. *Adv. Funct. Mater.* **2011**, *21*, 3938-3946

[74] X. Xia, Y. Wang, A. Ruditskiy, Y. Xia. *Adv. Mater.* **2013**, *25*, 6313-6333

[75] Z.-Y. Zhou, Z.-Z. Huang, D.-J. Chen, Q. Wang, N. Tian, S.-G. Sun. *Angew. Chem. Int. Ed.* **2010**, *49*, 411-414

[76] G. J. Leong, M. C. Schulze, M. B Strand, D. Maloney, S. L. Frisco, H. N. Dinh, B. Pivovar, R. M. Richards. *Appl. Organometal. Chem.* **2014**, *28*, 1-17

[77] N. Toshima, T. Yonezawa. *New J. Chem.* **1998**, *22*, 1179-1201

[78] Y. Sun. *Chem. Mater.* **2007**, *19*, 5845-5847

[79] Z. Li, C. V. Ciobanu, J. Hu, J.-P. Palomares-Báez, J.-L. Rodríguez-López, R. Richards. *Phys. Chem. Chem. Phys* **2011**, *13*, 2582-2589

[80] L. Chen, G. J. Leong, M. C. Schulze, H. N. Dinh, B. Pivovar, J. Hu, Z. Qi, Y. Fang, S. Prikhodko, M. Pozuelo, S. Kodambaka, R. M. Richards. *ChemCatChem* **2012**, *4*, 1662-1667

[81] G. J. Leong, A. Ebnonnasir, M. C. Schulze, M. B Strand, C. Ngo, D. Maloney, S. L. Frisco, H. N. Dinh, B. Pivovar, G. H. Gilmer, S. Kodambaka, C. V. Ciobanu, R. M. Richards. *Nanoscale* **2014**, *6*, 11364-11371

[82] B. S. Pivovar. *DOE Hydrogen and Fuel Cells Program Review* **2012**, 1-27

[83] A. Dursun, D. V. Pugh, S. G. Corcoran. *J. Electrochem Soc.* **2003**, *150*, B355-B360

[84] S. E. Skrabalak, J. Chen, Y. Sun, X. Lu, L. Au, C. M. Cobley, Y. Xia. *Acc. Chem. Res.* **2008**, *41*, 1587-1595

[85] L. Au, X. Lu, Y. Xia. *Adv. Mater.* **2008**, *20*, 2517-2522

[86] X. Lu, H.-Y. Tuan, J. Chen, Z.-Y. Li, B. A. Korgel, Y. Xia. *J. Am. Chem. Soc.* **2007**, *129*, 1733-1742

[87] Y. Yin, C. Erdonmez, S. Aloni, A. P. Alivisatos. *J. Am. Chem. Soc.* **2006**, *128*, 12671-12673

[88] C. Yu, S. Koh, J. E. Leisch, M. F. Toney, P. Strasser. *Faraday Discuss.* **2008**, *140*, 283-296

[89] Y. Sun, Y. Wang. *Nano Lett.* **2011**, *11*, 4386-4392

[90] B. Goris, L. Polavarapu, S. Bals, G. V. Tendeloo, L. M. Liz-Marzán. *Nano Lett.* **2014**, *14*, 3220-3226

[91] K. D. Gilroy, A. Sundar, P. Farzinpour, R. A. Hughes, S. Neretina. *Nano Res.* **2014**, *7*, 365-379

[92] B. S. Pivovar. *Annual Merit Review and Peer Evaluation Meeting* **2011**, 1-25

[93] B. S. Pivovar. *DOE Hydrogen and Fuel Cells Program Review* **2013**, 1-27

[94] J. Ilavsky, P. R. Jemian. *J. Appl. Cryst.* **2009**, *42*, 347-353

[95] D. Diercks, B. P. Gorman, C. L. Cheung, G. Wang. *Microsc. Microanal.* **2009**, 15 (Supplement S2), 254-255

[96] B. P. Gorman, D. R. Diercks, N. Salmon, E. Stach, G. Amador, C. Hartfield. *Microsc. oday* **2008**, 16, 42-47

[97] Z. Peng, H. Yang. *J. Solid State Chem.* **2008**, *181*, 1546-1551

[98] Y. Herbani, T. Nakamura, S. Sato. *J. Colloid Interface Sci.* **2012**, *375*, 78-87

[99] L. Vegard, H. Dale. *Z. Kristallogr.* **1928**, *67*, 148-161

APPENDIX A

PERMISSIONS FOR USE IN CHAPTERS 1 AND 5

A.1 Background

This appendix contains the rights retained by journal authors from Electrochemistry Communications and The Journal of Physical Chemistry C, as well as email correspondence from the coauthors granting permission for re-use of the publication as a chapter in this thesis.

A.2 Rights retained by journal authors

A.2.1 Chapter 1 – Electrochemistry Communications

This Agreement between Matthew Strand ("You") and Elsevier ("Elsevier") consists of your license details and the terms and conditions provided by Elsevier and Copyright Clearance Center.

License Number	4155570467060
License date	Jul 24, 2017
Licensed Content Publisher	Elsevier
Licensed Content Publication	Electrochemistry Communications
Licensed Content Title	Enhanced stability of Pt electrocatalysts by nitrogen doping in CNTs for PEM fuel cells
Licensed Content Author	Yougui Chen,Jiajun Wang,Hao Liu,Ruyin Li,Xueliang Sun,Siyu Ye,Shanna Knights
Licensed Content Date	Oct 1, 2009
Licensed Content Volume	11
Licensed Content Issue	10
Licensed Content Pages	6
Start Page	2071
End Page	2076
Type of Use	reuse in a thesis/dissertation
Portion	figures/tables/illustrations
Number of figures/tables/ illustrations	1
Format	both print and electronic
Are you the author of this Elsevier article?	No
Will you be translating?	No
Original figure numbers	2

Title of your thesis/ dissertation	DEVELOPMENT OF N-DOPED CARBON NANOMATERIALS WITH CONTROLLED SHAPE AND COMPOSITION FOR FUNDAMENTAL STUDIES OF ELECTROCATALYTIC SYSTEMS BASED ON PGM AND PGM-FREE CATALYSTS
Expected completion date	Jul-17

Terms and Conditions

INTRODUCTION

1. The publisher for this copyrighted material is Elsevier. By clicking "accept" in connection with completing this licensing transaction, you agree that the following terms and conditions apply to this transaction (along with the Billing and Payment terms and conditions established by Copyright Clearance Center, Inc. ("CCC"), at the time that you opened your Rightslink account and that are available at any time at http://myaccount.copyright.com).

GENERAL TERMS

2. Elsevier hereby grants you permission to reproduce the aforementioned material subject to the terms and conditions indicated.

3. Acknowledgement: If any part of the material to be used (for example, figures) has appeared in our publication with credit or acknowledgement to another source, permission must also be sought from that source. If such permission is not obtained then that material may not be included in your publication/copies. Suitable acknowledgement to the source must be made, either as a footnote or in a reference list at the end of your publication, as follows:

"Reprinted from Publication title, Vol /edition number, Author(s), Title of article / title of chapter, Pages No., Copyright (Year), with permission from Elsevier [OR APPLICABLE SOCIETY COPYRIGHT OWNER]." Also Lancet special credit - "Reprinted from The Lancet,

Vol. number, Author(s), Title of article, Pages No., Copyright (Year), with permission from Elsevier."

4. Reproduction of this material is confined to the purpose and/or media for which permission is hereby given.

5. Altering/Modifying Material: Not Permitted. However figures and illustrations may be altered/adapted minimally to serve your work. Any other abbreviations, additions, deletions and/or any other alterations shall be made only with prior written authorization of Elsevier Ltd. (Please contact Elsevier at permissions@elsevier.com). No modifications can be made to any Lancet figures/tables and they must be reproduced in full.

6. If the permission fee for the requested use of our material is waived in this instance, please be advised that your future requests for Elsevier materials may attract a fee.

7. Reservation of Rights: Publisher reserves all rights not specifically granted in the combination of (i) the license details provided by you and accepted in the course of this licensing transaction, (ii) these terms and conditions and (iii) CCC's Billing and Payment terms and conditions.

8. License Contingent Upon Payment: While you may exercise the rights licensed immediately upon issuance of the license at the end of the licensing process for the transaction, provided that you have disclosed complete and accurate details of your proposed use, no license is finally effective unless and until full payment is received from you (either by publisher or by CCC) as provided in CCC's Billing and Payment terms and conditions. If full payment is not received on a timely basis, then any license preliminarily granted shall be deemed automatically revoked and shall be void as if never granted. Further, in the event that you breach any of these terms and conditions or any of CCC's Billing and Payment terms and conditions, the license is

automatically revoked and shall be void as if never granted. Use of materials as described in a revoked license, as well as any use of the materials beyond the scope of an unrevoked license, may constitute copyright infringement and publisher reserves the right to take any and all action to protect its copyright in the materials.

9. Warranties: Publisher makes no representations or warranties with respect to the licensed material.

10. Indemnity: You hereby indemnify and agree to hold harmless publisher and CCC, and their respective officers, directors, employees and agents, from and against any and all claims arising out of your use of the licensed material other than as specifically authorized pursuant to this license.

11. No Transfer of License: This license is personal to you and may not be sublicensed, assigned, or transferred by you to any other person without publisher's written permission.

12. No Amendment Except in Writing: This license may not be amended except in a writing signed by both parties (or, in the case of publisher, by CCC on publisher's behalf).

13. Objection to Contrary Terms: Publisher hereby objects to any terms contained in any purchase order, acknowledgment, check endorsement or other writing prepared by you, which terms are inconsistent with these terms and conditions or CCC's Billing and Payment terms and conditions. These terms and conditions, together with CCC's Billing and Payment terms and conditions (which are incorporated herein), comprise the entire agreement between you and publisher (and CCC) concerning this licensing transaction. In the event of any conflict between your obligations established by these terms and conditions and those established by CCC's Billing and Payment terms and conditions, these terms and conditions shall control.

14. Revocation: Elsevier or Copyright Clearance Center may deny the permissions described in this License at their sole discretion, for any reason or no reason, with a full refund payable to you. Notice of such denial will be made using the contact information provided by you. Failure to receive such notice will not alter or invalidate the denial. In no event will Elsevier or Copyright Clearance Center be responsible or liable for any costs, expenses or damage incurred by you as a result of a denial of your permission request, other than a refund of the amount(s) paid by you to Elsevier and/or Copyright Clearance Center for denied permissions.

LIMITED LICENSE

The following terms and conditions apply only to specific license types:

15. Translation: This permission is granted for non-exclusive world English rights only unless your license was granted for translation rights. If you licensed translation rights you may only translate this content into the languages you requested. A professional translator must perform all translations and reproduce the content word for word preserving the integrity of the article.

16. Posting licensed content on any Website: The following terms and conditions apply as follows: Licensing material from an Elsevier journal: All content posted to the web site must maintain the copyright information line on the bottom of each image; A hyper-text must be included to the Homepage of the journal from which you are licensing at http://www.sciencedirect.com/science/journal/xxxxx or the Elsevier homepage for books at http://www.elsevier.com; Central Storage: This license does not include permission for a scanned version of the material to be stored in a central repository such as that provided by Heron/XanEdu.

Licensing material from an Elsevier book: A hyper-text link must be included to the Elsevier homepage at http://www.elsevier.com . All content posted to the web site must maintain the copyright information line on the bottom of each image.

Posting licensed content on Electronic reserve: In addition to the above the following clauses are applicable: The web site must be password-protected and made available only to bona fide students registered on a relevant course. This permission is granted for 1 year only. You may obtain a new license for future website posting.

17. For journal authors: the following clauses are applicable in addition to the above:

Preprints:

A preprint is an author's own write-up of research results and analysis, it has not been peer-reviewed, nor has it had any other value added to it by a publisher (such as formatting, copyright, technical enhancement etc.).

Authors can share their preprints anywhere at any time. Preprints should not be added to or enhanced in any way in order to appear more like, or to substitute for, the final versions of articles however authors can update their preprints on arXiv or RePEc with their Accepted Author Manuscript (see below).

If accepted for publication, we encourage authors to link from the preprint to their formal publication via its DOI. Millions of researchers have access to the formal publications on ScienceDirect, and so links will help users to find, access, cite and use the best available version. Please note that Cell Press, The Lancet and some society-owned have different preprint policies. Information on these policies is available on the journal homepage.

Accepted Author Manuscripts: An accepted author manuscript is the manuscript of an article that has been accepted for publication and which typically includes author-incorporated changes suggested during submission, peer review and editor-author communications.

Authors can share their accepted author manuscript:

- Immediately

    - via their non-commercial person homepage or blog
    - by updating a preprint in arXiv or RePEc with the accepted manuscript
    - via their research institute or institutional repository for internal institutional uses or as part of an invitation-only research collaboration work-group
    - directly by providing copies to their students or to research collaborators for their personal use
    - for private scholarly sharing as part of an invitation-only work group on commercial sites with which Elsevier has an agreement
- After the embargo period
    - via non-commercial hosting platforms such as their institutional repository
    - via commercial sites with which Elsevier has an agreement

In all cases accepted manuscripts should:

- link to the formal publication via its DOI
- bear a CC-BY-NC-ND license - this is easy to do
- if aggregated with other manuscripts, for example in a repository or other site, be shared in alignment with our hosting policy not be added to or enhanced in any way to appear more like, or to substitute for, the published journal article.

Published journal article (JPA): A published journal article (PJA) is the definitive final record of published research that appears or will appear in the journal and embodies all value-adding publishing activities including peer review co-ordination, copy-editing, formatting, (if relevant) pagination and online enrichment.

Policies for sharing publishing journal articles differ for subscription and gold open access articles:

Subscription Articles: If you are an author, please share a link to your article rather than the full-text. Millions of researchers have access to the formal publications on ScienceDirect, and so links will help your users to find, access, cite, and use the best available version.

Theses and dissertations which contain embedded PJAs as part of the formal submission can be posted publicly by the awarding institution with DOI links back to the formal publications on ScienceDirect.

If you are affiliated with a library that subscribes to ScienceDirect you have additional private sharing rights for others' research accessed under that agreement. This includes use for classroom teaching and internal training at the institution (including use in course packs and courseware programs), and inclusion of the article for grant funding purposes.

Gold Open Access Articles: May be shared according to the author-selected end-user license and should contain a CrossMark logo, the end user license, and a DOI link to the formal publication on ScienceDirect.

Please refer to Elsevier's posting policy for further information.

18. For book authors the following clauses are applicable in addition to the above: Authors are permitted to place a brief summary of their work online only. You are not allowed to download and post the published electronic version of your chapter, nor may you scan the printed edition to create an electronic version. Posting to a repository: Authors are permitted to post a summary of their chapter only in their institution's repository.

19. Thesis/Dissertation: If your license is for use in a thesis/dissertation your thesis may be submitted to your institution in either print or electronic form. Should your thesis be published commercially, please reapply for permission. These requirements include permission for the Library and Archives of Canada to supply single copies, on demand, of the complete thesis and

include permission for Proquest/UMI to supply single copies, on demand, of the complete thesis. Should your thesis be published commercially, please reapply for permission. Theses and dissertations which contain embedded PJAs as part of the formal submission can be posted publicly by the awarding institution with DOI links back to the formal publications on ScienceDirect.

Elsevier Open Access Terms and Conditions

You can publish open access with Elsevier in hundreds of open access journals or in nearly 2000 established subscription journals that support open access publishing. Permitted third party re-use of these open access articles is defined by the author's choice of Creative Commons user license. See our open access license policy for more information.

Terms & Conditions applicable to all Open Access articles published with Elsevier:

Any reuse of the article must not represent the author as endorsing the adaptation of the article nor should the article be modified in such a way as to damage the author's honour or reputation. If any changes have been made, such changes must be clearly indicated.

The author(s) must be appropriately credited and we ask that you include the end user license and a DOI link to the formal publication on ScienceDirect.

If any part of the material to be used (for example, figures) has appeared in our publication with credit or acknowledgement to another source it is the responsibility of the user to ensure their reuse complies with the terms and conditions determined by the rights holder.

Additional Terms & Conditions applicable to each Creative Commons user license:

CC BY: The CC-BY license allows users to copy, to create extracts, abstracts and new works from the Article, to alter and revise the Article and to make commercial use of the Article (including reuse and/or resale of the Article by commercial entities), provided the user gives

- Systematic distribution via e-mail lists or share buttons
- Posting or linking by commercial companies for use by customers of those companies

A.2.2 Chapter 5 – The Journal of Physical Chemistry C

Permission/license is granted for your order at no charge.

This type of permission/license, instead of the standard Terms & Conditions, is sent to you because no fee is being charged for your order. Please note the following:

- Permission is granted for your request in both print and electronic formats, and translations.
- If figures and/or tables were requested, they may be adapted or used in part.
- Please print this page for your records and send a copy of it to your publisher/graduate school.
- Appropriate credit for the requested material should be given as follows: "Reprinted (adapted) with permission from (COMPLETE REFERENCE CITATION). Copyright (YEAR) American Chemical Society." Insert appropriate information in place of the capitalized words.
- One-time permission is granted only for the use specified in your request. No additional uses are granted (such as derivative works or other editions). For any other uses, please submit a new request

A.3 Email correspondence from coauthors for Chapter 5

Emails from co-authors were received in response to the following email sent on 26 May 2017: “Dear all, If you are receiving this message, I require a response from you. I wish to re-use part or all of the publication Mechanistic Study of Shape-Anisotropic Nanomaterials Synthesized

via Spontaneous Galvanic Displacement, and to comply with current protocols for including published material in a thesis, I am required to obtain written consent from all coauthors. Can you all reply to me with your consent? Here's an example response: "I, [your name], hereby authorize Matthew B Strand to use any part or all of DOI: 10.1021/acs.jpcc.6b07363 in his published thesis." Thank you for your time, Matthew Strand" 26 May 2017, 8:33 AM

The responses received to the email were as follows:

"I authorize." from Ryan M. Richards, 26 May 2017, 8:52 AM

"I, David R. Diercks, hereby authorize Matthew B Strand to use any part or all of DOI: 10.1021/acs.jpcc.6b07363 in his published thesis." 26 May 2017, 8:55 AM

"I, Bryan Pivovar, hereby authorize Matthew B Strand to use any part or all of DOI: 10.1021/acs.jpcc.6b07363 in his published thesis." 26 May 2017, 8:58 AM

"I approve." from Brian Gorman, 26 May 2017, 8:59 AM

"Dear Matthew, Congratulations! "I, G. Jeremy Leong, hereby authorize Matthew B Strand to use any part or all of DOI: 10.1021/acs.jpcc.6b07363 in his published thesis." Thanks, G. Jeremy Leong" 27 May 2017, 5:29 PM

"Matthew, I authorize your usage. Official statement below: "I, BRIAN LARSEN, hereby authorize Matthew B Strand to use any part or all of DOI: 10.1021/acs.jpcc.6b07363 in his published thesis." Good luck with your thesis. Best, Brian" 29 May 2017, 6:54 PM

"I, Christopher J. Tassone, hereby authorize Matthew B Strand to use any part or all of DOI: 10.1021/acs.jpcc.6b07363 in his published thesis." 1 June 2017, 9:00 AM

"I, Svitlana Pylypenko, hereby authorize Matthew B Strand to use any part or all of DOI: 10.1021/acs.jpcc.6b07363 in his published thesis." 6 June 2017, 9:19 AM

"Matt, Congratulations on your thesis defense. I apologize for the lateness of my response, thanks for the reminders. Your request is below. I, Kenneth Neyerlin, hereby authorize Matthew B Strand to use any part or all of DOI: 10.1021/acs.jpcc.6b07363 in his published thesis. Best, KC." 15 June 2017, 10:15 AM